

Two MODIS Aerosol Products over Ocean on the *Terra* and *Aqua* CERES SSF Datasets

ALEXANDER IGNATOV,^{*} PATRICK MINNIS,⁺ NORMAN LOEB,[#] BRUCE WIELICKI,⁺ WALTER MILLER,[@]
SUNNY SUN-MACK,[@] DIDIER TANRÉ,[&] LORRAINE REMER,^{**} ISTVAN LASZLO,^{*} AND ERIKA GEIER⁺

^{*} NOAA/NESDIS/Office of Research and Applications, Camp Springs, Maryland

⁺ Atmospheric Sciences, NASA Langley Research Center, Hampton, Virginia

[#] Center for Atmospheric Sciences, Hampton University, Hampton, Virginia

[@] Science Applications International Corporation, Hampton, Virginia

[&] Laboratoire d'Optique Atmosphérique, Université des Sciences et Technologies de Lille, Villeneuve d'Ascq, France

^{**} NASA Goddard Space Flight Center, Greenbelt, Maryland

(Manuscript received 8 August 2003, in final form 25 June 2004)

ABSTRACT

Understanding the impact of aerosols on the earth's radiation budget and the long-term climate record requires consistent measurements of aerosol properties and radiative fluxes. The Clouds and the Earth's Radiant Energy System (CERES) Science Team combines satellite-based retrievals of aerosols, clouds, and radiative fluxes into Single Scanner Footprint (SSF) datasets from the *Terra* and *Aqua* satellites. Over ocean, two aerosol products are derived from the Moderate Resolution Imaging Spectroradiometer (MODIS) using different sampling and aerosol algorithms. The *primary*, or M, product is taken from the standard multispectral aerosol product developed by the MODIS aerosol group while a simpler, *secondary* [Advanced Very High Resolution Radiometer (AVHRR) like], or A, product is derived by the CERES Science Team using a different cloud clearing method and a single-channel aerosol algorithm. Two aerosol optical depths (AOD), τ_{A1} and τ_{A2} , are derived from MODIS bands 1 (0.644 μm) and 6 (1.632 μm) resembling the AVHRR/3 channels 1 and 3A, respectively. On *Aqua* the retrievals are made in band 7 (2.119 μm) because of poor quality data from band 6. The respective Ångström exponents can be derived from the values of τ . The A product serves as a backup for the M product. More importantly, the overlap of these aerosol products is essential for placing the 20+ year heritage AVHRR aerosol record in the context of more advanced aerosol sensors and algorithms such as that used for the M product.

This study documents the M and A products, highlighting their CERES SSF specifics. Based on 2 weeks of global *Terra* data, coincident M and A AODs are found to be strongly correlated in both bands. However, both domains in which the M and A aerosols are available, and the respective τ/α statistics significantly differ because of discrepancies in sampling due to differences in cloud and sun-glint screening. In both aerosol products, correlation is observed between the retrieved aerosol parameters (τ/α) and ambient cloud amount, with the dependence in the M product being more pronounced than in the A product.

1. Introduction

Aerosols have an important, yet somewhat uncertain, impact on the earth's radiation budget and climate. Determining that impact on the climate record requires consistent measurements of aerosol properties and radiative fluxes. To that end, three satellites, the Tropical Rainfall Measuring Mission (TRMM), *Terra*, and *Aqua* (launched in November 1997, December 1999, and May 2002, respectively), carry a total of five Clouds and the Earth's Radiant Energy System (CERES) instruments to measure the radiant energy exchange on Earth

(Wielicki et al. 1996). The TRMM satellite carries the CERES protoflight model (PFM); *Terra* carries flight models 1 and 2 (FM1–2); and *Aqua* carries flight models 3 and 4 (FM3–4). The Single Scanner Footprint (SSF) products (Geier et al. 2003) combine the CERES data with cloud and aerosol retrievals from the Visible and Infrared Scanner (VIRS) on TRMM and the Moderate Resolution Imaging Spectroradiometer (MODIS) on *Terra* and *Aqua*. The spatial resolution is ~ 2 km at nadir for VIRS, and 0.25–1 km for MODIS. The SSF retains the mean and standard deviation of the imager pixel radiances and cloud/aerosol retrievals separately for the clear and cloudy portions of every CERES field of view (FOV). The spatial resolution for CERES (equivalent diameter at nadir) is ~ 10 km on TRMM and ~ 20 km on *Terra* and *Aqua*. Aerosol retrievals on the SSF have proven useful for a number of applica-

Corresponding author address: Dr. Alex Ignatov, E/RA1, Rm. 603, 5200 Auth Road, Camp Springs, MD 20746-4304.
E-mail: Alex.Ignatov@noaa.gov

tions, such as estimating the surface and atmospheric radiation balance (Charlock et al. 2002) and studies on top-of-atmosphere (TOA) aerosol radiative forcing (Loeb and Kato 2002) and molecular albedo (Kato et al. 2002).

This study documents two aerosol products available over ocean on the *Terra* and *Aqua* CERES SSFs and compares them using 2 weeks of global *Terra* data from 15–21 December 2000 and 1–7 June 2001 (hereafter December 2000 and June 2001). Note that the *Aqua* CERES SSF data are also documented here, but they were not available for science analyses at the time of this writing. The TRMM CERES SSF contains only one aerosol product based on VIRS data and is analyzed elsewhere (A. Ignatov et al. 2005, unpublished manuscript).

The *primary*, M, aerosol product on the CERES SSF is generated by subsetting and remapping the MOD04 (*Terra*; MYD04 on *Aqua*) granules onto CERES footprints. The MOD04 product uses sophisticated cloud screening and aerosol retrieval algorithms developed by the MODIS cloud and aerosol groups¹ (Tanré et al. 1997; Ackerman et al. 1998; Martins et al. 2002; Remer et al. 2005, hereafter REM). In this study, only two M aerosol optical depths, τ_{M1} and τ_{M2} , are used at the centroid wavelengths of MODIS bands 1 ($\lambda_1=0.644 \mu\text{m}$) and 6 ($\lambda_2=1.632 \mu\text{m}$). On *Aqua*, AOD in band 7 ($\lambda_2=2.119 \mu\text{m}$) is used for τ_{M2} due to poor quality of band 6 (C. Moeller 2003, personal communication). The respective Ångström exponent is derived as $\alpha_M = -\ln(\tau_{M1}/\tau_{M2})/\ln(\lambda_1/\lambda_2)$.

The *secondary* A product uses complex, but different, glint and cloud screening criteria and a simpler [Advanced Very High Resolution Radiometer (AVHRR)-like] third-generation aerosol algorithm (Ignatov and Stowe 2002a; Ignatov et al. 2004). Two AODs, τ_{A1} (0.630 μm) and τ_{A2} (1.610 μm) [τ_{A2} (2.119 μm) on *Aqua*], are derived from MODIS bands 1 and 6 (7 on *Aqua*) using single-channel algorithms and reported at the wavelengths representative of band centers for a generic AVHRR or VIRS sensor. Using a standard set of reference wavelengths ensures compatibility of the respective A products derived from a variety of sensors (AVHRR, VIRS, and MODIS) flown on board different platforms [National Oceanic and Atmospheric Administration (NOAA), TRMM, *Terra*, and *Aqua*]. Cross-platform differences in the A products, if observed, are then due to either different sampling of aerosol pixels (specified by domain of sun-view-scatter-glint geometry, resulting from the platform's orbital configuration, and cloud/glint screening),

different radiometric performance of the sensors, or both.

The availability of the two aerosol products on the CERES SSF side by side is helpful to place long-term time series of the heritage A products from NOAA/AVHRR (20+ yr) and TRMM/VIRS (6+ yr) in the context of more accurate M-aerosol retrievals, and to quickly assess the improvements provided by the multichannel MODIS. Ultimately, these analyses provide a useful insight into the current status of aerosol retrievals from space and serve to highlight and prioritize outstanding issues.

2. M- and A-aerosol production over ocean on the *Terra* and *Aqua* CERES SSFs

The first step of the SSF processing includes subsampling of MODIS pixels (nominal resolution at nadir ~ 1 km). On the *Terra* CERES SSF Edition 1A (used in this study), every other pixel/line is sampled, effectively reducing the data volume by a factor of 4. [In the latest version of the SSF software, used in generation of *Terra* Edition 2 and *Aqua* Edition 1, every fourth (4) pixel in every other (2) line is subsampled, thereby reducing the data volume by a factor of 8.] The second step is assigning aerosol properties from both the MOD04 and A products (when available) to the respective subsampled MODIS pixels. The third step is convolving these subsampled pixel aerosol properties into the corresponding CERES footprint using the CERES point spread function (Geier et al. 2003), to provide an optimal match between the radiative fluxes and aerosol information.

The CERES SSF aerosol processing is succinctly summarized in Table 1. Note that both M and A products are reported only at solar zenith angles $\theta_o < 70^\circ$. Below, only brief explanations are given. For detail, the reader is advised to check with the references cited throughout this section and in Table 1.

a. M processing

Of the 47 MOD04 ocean and land aerosol parameters, 13 ocean and 11 land aerosol parameters are first selected. The selected parameters are then spread to each subsampled MODIS pixel found within the MOD04 granule (with nominal resolution at nadir 10 km). Finally, all subsampled MODIS pixels are averaged into CERES footprints (with nominal resolution at nadir ~ 20 km) and weighted by the CERES point spread function. This convolved average of the MOD04 parameters in each SSF constitutes the M product.

The MOD04 processing (Tanré et al. 1997; REM) at the NASA Goddard Space Flight Center (GSFC) Distributed Active Archive Center is performed in groups of 20×20 MODIS geolocated pixel reflectances, $\rho_{EV} \mu_o$ (see appendix A for definitions) at a nominal 500-m resolution, each cluster resulting in one MOD04 granule. The MODIS aerosol bands 1–7 were carefully se-

¹ MOD04 processing evolves continuously. Collection 003 was used in the *Terra* SSF Edition 1A product analyzed in this study. As of the time of this revision, *Terra* Edition 2 and *Aqua* Edition 1 CERES SSF products became available based on collection 004 data, and development of collection 005 is underway.

TABLE 1. Aerosol production over oceans on the *Terra* and *Aqua* CERES SSF datasets. In the table, LaRC: Langley Research Center.

Attribute	M product	A product
Designation on dataset	Primary	Secondary
Data flow	Produced: NASA GSFC; mapped: NASA LaRC	Produced: NASA LaRC; mapped: NASA LaRC
Generating	NASA GSFC: ($20 \times 20 \times 500$ m/ L1b SE-normalized <i>reflectance</i>) \rightarrow Correct for $H_2O/O_3/CO_2$ absorption \rightarrow Screen cloud/sediment/glint \rightarrow Make aerosol retrievals \rightarrow (Average 25%–75%, $N \geq 10$) \rightarrow Report aerosols at $(10 \text{ km})^2$	NASA LaRC: [MOD021km/L1b <i>radiance</i>] \rightarrow Sample every 2d pixel/line \rightarrow Screen cloud/glint \rightarrow Uniformity/adjacency tests \rightarrow Report radiances/geometries at $(2 \text{ km})^2$
NASA LaRC: CERES footprints: mapping/retrievals	Average aerosol products \rightarrow Report on CERES SSF	Average radiances/geometries \rightarrow Normalize to solar flux/SE distance \rightarrow Make aerosol retrievals \rightarrow Report on CERES SSF
Nonaerosol pixels	Summary: REM	Summary: Ignatov et al. (2005, unpublished manuscript)
Cloud	Ackerman et al. (1998); Martins et al. (2002)	Trepte et al. (1999); Minnis et al. (2004, unpublished manuscript)
Turbid water/case 2	Li et al. (2003)	None
Glint	Glint angle, $\gamma > 40^\circ$	$\gamma > 40^\circ$ and antisolar side of orbit
Aerosol algorithm	NASA GSFC MODIS Aerosol Group (version 3) (Tanré et al. 1997; Levy et al. 2003; REM)	NOAA/NESDIS “AVHRR-like” algorithm (3d generation) (Ignatov and Stowe 2002a; Ignatov et al. 2004)
Spectral	Multichannel in bands: <i>Terra</i> (6): 1–2, 4–7 ($0.553\text{--}2.119 \mu\text{m}$) <i>Aqua</i> (5): 1–2, 5–7 (6: $1.632 \mu\text{m}$ not used)	Single channel in bands: <i>Terra</i> : 1 (0.644) and 6 ($1.632 \mu\text{m}$) <i>Aqua</i> : 1 (0.644) and 7 ($2.119 \mu\text{m}$)
Aerosol model	Bilognormal 4 fine/5 coarse modes. Solves for: fine/coarse mode; $\tau_{0.553}$; Mode ratio, $\eta_{0.553}$; Eff. radius, r_{eff} .	Monolognormal/fixed modes. Solves for $\tau_{0.63}$ and $\tau_{1.61}$ independently in bands.
RTM	Ahmad–Fraser (1982) vector	6S scalar (Vermote et al. 1997)
Surface (bidirectional)	Cox–Munk (1954b) isotropic ($V = 6 \text{ m s}^{-1}$)	Cox–Munk (1954a) anisotropic ($V = 1 \text{ m s}^{-1}$)
Surface (Lambertian)	0.553: 0.5%; 0.644–2.119: 0.0%	0.644: 0.2%; 1.632/2.119: 0.0%
Handling spectral filters	Monochrome, λ_{eff} (0.466, 0.553, 0.644, 0.855, 1.243, 1.632, 2.119)	Integration/convolution
Lookup tables	7 bands (1–7); $16\theta = 0(6)88.5^\circ$; $15\theta_0 = 1.5(6)72^\circ$; $16\phi = 1.5(12)180^\circ$; $6\tau = 0, 0.2, 0.5, 1.0, 2.0, 3.0$; 9 modes = 4 fine + 5 coarse	2 LUTs/bands (1 and 6/7); $13\theta = 0(6)72^\circ$; $13\theta_0 = 0(6)72^\circ$; $19\phi = 0(10)180^\circ$; $6\tau = 0, 0.15, 0.30, 0.60, 1.20, 1.50$
Reflectances	Calculated at λ_{eff}	Convolution
Rayleigh optical depth	Calculated at λ_{eff} /built in LUT	Convolution/built in LUT (Table A3)
Gaseous absorption	Reflectances corrected/not built in LUT	Convolution/built in LUT (Table A3)

lected to minimize gaseous absorption, but some absorption effects remain (see Table A3 in appendix A). In the MOD04 processing, the reflectances are first corrected for gaseous absorption. Concentrations of water vapor (H_2O), ozone (O_3), and carbon dioxide (CO_2) are specified from either the NOAA/National Centers for Environmental Prediction (NCEP) forecast (H_2O and O_3) or from climatology (CO_2). Note that the effect not only depends upon the amount of gas, but also is a function of the Rayleigh scattering, gaseous absorption, and aerosol extinction relative vertical distribution. The correction equations were derived assuming midlati-

tude summer vertical profiles for gases and $\sim 2 \text{ km}$ scaling factor for aerosol vertical distribution (REM).

Next, pixels over water are identified, and the cloud mask and sediment tests are applied. The primary cloud test differentiates by spatial uniformity. The standard deviation of $0.553\text{-}\mu\text{m}$ reflectances in a 3×3 array of pixels must be $< 2.5 \times 10^{-3}$ (0.25%) for the center pixel to be used in the retrieval. Otherwise the pixel is rejected (Martins et al. 2002). The other tests include thresholds in the visible reflectance ($0.466 \mu\text{m}$) and seven individual tests from the standard cloud mask (Ackerman et al. 1998). The sediment test takes advan-

tage of the strong absorption by water beyond 1 μm (Li et al. 2003). Pixels that pass all tests are sorted by reflectance at 0.855 μm , and the lower and upper 25% are excluded. If the central 50% include at least 10 pixels within the 20×20 window, the reflectances in each of the seven MODIS bands 1–7 (from 0.466 to 2.119 μm) are averaged and checked if outside the glint area ($\gamma > 40^\circ$) and internally consistent.

Aerosol lookup tables (LUTs) are applied to the average reflectances in only six (1–2 and 4–7 on *Terra*) or five bands (1–2, 4–5, and 7 on *Aqua*) ranging from ~ 0.55 to 2.1 μm . Band 3 (0.47 μm) is not used because of its response to materials like phytoplankton beneath the ocean surface. AOD for band 3 is modeled from the other bands. Retrieved AODs are reported in all seven bands 1–7 ranging from ~ 0.47 to 2.1 μm . The aerosol size distribution is assumed to be a mix of two fractions—fine and coarse—each being represented by a single lognormal mode. The algorithm chooses one fine (out of four) and one coarse (out of five) mode and solves for their ratio and aerosol concentration. The surface characteristics follow the isotropic Cox and Munk (1954b) model with a wind speed 6 m s^{-1} . Aerosol inversions are made with nine five-dimensional LUTs, one for each aerosol mode: 15 view zenith angles, 15 sun zenith angles, 46 relative azimuth angles, and 4 AODs in six bands. In the error minimization procedure, linear mixtures of different pairs of fine and coarse modes are tested, with different weights. The LUTs have been precalculated using the Ahmad–Fraser (1982) vector code at the six monochromatic wavelengths, for the atmosphere containing molecules and aerosols and bounded by a rough ocean surface from below.

b. A processing

Two elements of the A-product processing, data flow and screening nonaerosol pixels, are detailed in Minnis et al. (1999, 2004, unpublished manuscript) and Trepte et al. (1999) (and summarized by Ignatov et al. 2005, unpublished manuscript). The other three elements— aerosol algorithm, radiative transfer model, LUTs—are identical to the third-generation AVHRR algorithm documented in (Ignatov and Stowe 2002a; Ignatov et al. 2004). The A processing uses MODIS radiances, L_{EV} , at the 1-km resolution (MOD02 1-km product, see appendix A for definitions), subsampled to every second line/pixel, effectively reducing the data volume by a factor of 4. To be used for aerosol retrievals a pixel must be over water, away from sun glint, cloud free, and pass uniformity and adjacency aerosol tests. Cloud screening involves a sequence of three cascading threshold tests. The measured reflectance at 0.644 μm and brightness temperatures at 3.7, 11, and 12 μm , and different combinations thereof, are compared with their *expected* values (Trepte et al. 1999). The expected values are specified as functions of geographical location, time, and illumination–observation geometry,

based upon analytical expressions, radiative transfer calculations, empirical models, atmospheric corrections, and interpolations. The difference or ratio between the measured and expected values is compared with a threshold estimated as a function of sun-view geometry by trial and error, from comparisons of predicted and observed clear values and from efforts to minimize the view angle dependence of the retrieved cloud amount. The most critical tests for aerosol retrievals are the uniformity and adjacency tests. The uniformity test is applied to sets of four clear pixels in a 2×2 subsampled array mentioned at the start of section 2. The difference between the maximum and minimum reflectance at 0.644 μm must be less than 3×10^{-3} (0.3%). The adjacency test further requires that all eight pixels surrounding a candidate pixel are clear. In addition to the $\gamma > 40^\circ$ threshold, the A-product glint identification requires that all pixels on the solar side of the orbit are excluded. (This convention is currently being reevaluated.) Reflectances in all cloud/glint-free MODIS pixels within a CERES footprint are averaged as explained in Geier et al. (2003).

AODs in bands 1 and 6 (7 for *Aqua*), τ_{A1} and τ_{A2} , are estimated assuming that aerosol microphysics and all nonaerosol factors are fixed and invariant over global oceans (Ignatov et al. 2004). Single-channel Second Simulation of the Satellite Signal in the Solar Spectrum (6S) radiative transfer model (RTM)-based (Vermote et al. 1997) LUTs were constructed as described by Ignatov and Stowe (2002a) for the average MODIS relative spectral response functions (see Fig. A1 in appendix A) and applied to the CERES-footprint average cloud-free reflectances, ρ . The resulting retrieved τ are reported at the centroid wavelengths of $\lambda_1 = 0.63$ and $\lambda_2 = 1.61$ μm ($\lambda_2 = 2.119$ μm for *Aqua*). Note that the reference wavelengths in the A product slightly differ from λ_{eff} in the M product. For the τ comparisons in this study, τ_A available on the CERES SSF datasets have been rescaled to the wavelengths at which the τ_M are reported as follows: $\tau_{A1}(0.644 \mu\text{m}) = 0.96377 \tau_{A1}(0.630 \mu\text{m})$ and $\tau_{A2}(1.632 \mu\text{m}) = 0.96716 \tau_{A2}(1.610 \mu\text{m})$. (Note that no scaling is needed for the τ_{A2} on *Aqua*.) The Ångström exponent is derived from rescaled τ as follows:

$$\alpha = \Lambda \times \ln(\tau_1/\tau_2), \quad \Lambda \equiv - \frac{1}{\ln(\lambda_1/\lambda_2)}. \quad (1)$$

Note that the τ_A -to- τ_M conversion factors are close to unity (within $\sim 3.5\%$) due to the proximity of λ_{eff} used in the A and M products. Their further refinement is possible based on the estimated Ångström exponent, but its effect on the accuracy of the scaling is negligible. The spectral amplification factor in Eq. (1), Λ , is $\Lambda \approx 1.08$ for bands 1 and 6 ($\lambda_1=0.644$, $\lambda_2=1.632$ μm), and $\Lambda \approx 0.83$ for bands 1 and 7 ($\lambda_1=0.644$, $\lambda_2=2.119$ μm).

TABLE 2. Aerosol products on the *Terra* and *Aqua* CERES SSF datasets.

Ocean (M product)	Ocean (A product)	Land (M product)
	Total count of MODIS pixels in a CERES FOV, $A-N_T$	
% cloud fraction in a CERES FOV, $M-F_C$ (%)	% cloud fraction in a CERES FOV, $A-F_C$ (%)	% cloud fraction in a CERES FOV
% of CERES FOV with aerosol, $M-F_A$ (%)	% of CERES FOV with aerosol, $A-F_A$ (%)	% of CERES FOV with aerosol
$\tau_M@466$ nm		$\tau@466$ nm
$\tau_M@553$ nm		$\tau@553$ nm
$\tau_M@644$ nm	$\tau_A@630$ nm	$\tau@644$ nm
$\tau_M@865$ nm	A—Aerosol radiance @630 nm	Mean reflectance @466 nm
$\tau_M@1243$ nm		Mean reflectance @644 nm
$\tau_M@1632$ nm	$\tau_A@1610$ nm (<i>Terra</i>)	Mean reflectance @865 nm
	A—Aerosol radiance @1610 nm (<i>Terra</i>)	
$\tau_M@2119$ nm	$\tau_A@2119$ nm (<i>Aqua</i>)	Mean reflectance @2130 nm
	A—Aerosol radiance @2119 nm (<i>Aqua</i>)	
M-solution index (small fraction)		Mean reflectance @3750 nm
M-solution index (large fraction)		Std dev reflectance @466 nm
$\tau_M@553$ nm (small fraction)		Aerosol types
$\tau_M@865$ nm (small fraction)		Dust weighting factor
$\tau_M@2119$ nm (small fraction)		Number of pixels (percentile)
M-cloud condensation nuclei (CCN)		

c. M- and A-aerosol products on the CERES SSF

Table 2 lists all of the aerosol and related ancillary parameters available on the *Terra* and *Aqua* CERES SSF datasets. The physical meaning of each is either self-explained, discussed below, or found in Kaufman et al. (1997), Tanré et al. (1997), REM, and Geier et al. (2003). Mapping specifics of the M- and A-aerosol products on the CERES SSF are summarized in appendix B.

The aerosol radiances used to retrieve the MOD04 τ_M over ocean were not saved, even though the τ_M in all seven MODIS bands are retained. (Note that the aerosol reflectances were saved in the land M product, which is not analyzed in this study.) In contrast, the A product reports τ_A in only two bands and retains the aerosol radiances. Offline testing of a new aerosol algorithm with the CERES SSF data is thus possible for the A product but not for the M product. In addition to τ_M , the M product over ocean includes other parameters that are listed in Table 2 but not used in this analysis. In this study, three M and A counterparts are analyzed: τ_{A1} versus τ_{M1} , τ_{A2} versus τ_{M2} , and α_A versus α_M .

Ancillary data listed in the first two lines of Table 2 include cloud amount, F_C (percent), and aerosol fraction, F_A (percent), in each CERES footprint. In addition, the A product provides a total count of MODIS pixels in a CERES FOV, N_T (no M-product counterpart is available for the $A-N_T$ parameter). In the preliminary analyses below, only the A-product parameters are used (cloud fraction, F_C , and aerosol pixel count, $N_A = N_T \times F_A / 100\%$). The M-product parameters will be explored in future work.

3. Preliminary evaluation of the M and A products on *Terra* CERES SSFs

Differences between the M and A products on the CERES SSFs are expected because of 1) different sampling (cloud and glint screening); 2) different aerosol algorithms (including different treatment of aerosol microphysics, Rayleigh scattering, gaseous absorption, surface reflectance, radiative transfer model used to generate the lookup tables, and numerical inversion methods); and 3) different propagation of data errors resulting from sensor calibration and other radiometric uncertainties in the M and A products. In this section, the two products are compared and their observed differences are discussed in terms of the potential error sources, 1, 2, and 3.

a. Defining the M and A (sub)samples: Statistics for December 2000 and June 2001

Statistics superimposed in Fig. 1 show that there are from ~ 2.2 to 2.3 million CERES footprints with at least one M- or A-aerosol retrieval in December 2000 and from 2.5 to 2.6 million in June 2001. Hereafter, these datasets are referred to as the MA union samples, or $M \oplus A \equiv A \oplus M$, and are considered =100%, by definition. In a union sample, there are some CERES FOVs in which *both* M- and A-product retrievals are available. They form a subsample that is termed the MA intersection: $M \otimes A \equiv A \otimes M$. Figure 1 shows that the MA intersection accounts for $\sim 45\%$ of the union sample. In some CERES FOVs, only the M retrievals are available (but the A retrievals are not); this

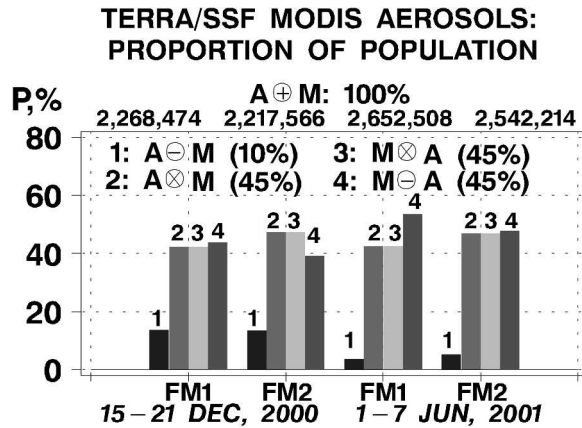


FIG. 1. Count of CERES footprints with valid aerosol retrievals in four datasets: December 2000 and June 2001, FM1 and FM2. The union sample, $M \oplus A$ (defined as 100%) consists of all FOVs in which either M- or A-aerosol retrievals are available. (Corresponding counts of CERES FOVs are listed in the top of the figure.) The intersection sample, $M \otimes A$ (~45% of the union sample, on average), consists of all FOVs in which both M- and A-aerosol retrievals are available. The M complement, $M \ominus A$ (~45% of the union sample, on average) consists of all FOVs in which the M retrievals are available but the A retrievals are not. The A complement, $A \ominus M$ (~10% of the union sample, on average), consists of all FOVs in which the A retrievals are available but the M retrievals are not.

subset is called the M complement, or $M \ominus A$. Likewise, the footprints having only A retrievals (but not M retrievals) form the A complement, or $A \ominus M$. The M and A complements account for another ~45% and ~10% of the union sample, respectively. The M and A complements highlight the effect of different sampling procedures (glint screening and cloud clearing) on the retrievals, whereas the MA intersection can be used to examine the effect of the aerosol algorithm differences.

The MA intersection and the M and A complements divide the union sample into three nonoverlapping subsamples from which other subsets can be constructed. In particular, the full M sample (referred to as the “M product”) comprises all footprints with valid M retrievals, regardless of A product availability. It is thus defined as a union of the MA intersection and the M complement: $M \equiv (M \otimes A) \oplus (M \ominus A)$ and accounts for ~90% of the union sample. Likewise, the full A sample (the “A product”) is a union of the MA intersection and A complement, $A \equiv (M \otimes A) \oplus (A \ominus M)$ and accounts for only ~55% of the union sample. The large difference between the M and A samples mainly results from excluding the solar side of the orbit in the A product processing.

b. M- and A-aerosol retrievals: Global distribution in different samples

Figure 2 plots the global distribution of τ_1 in December 2000 for the M and A products (columns) in the three subsamples (rows). Figures 2a(1) and 2b(1) re-

flect the M or A products (i.e., full M and A samples). The similarity between the two patterns is quite impressive, considering the large differences in the processing procedures. Aerosol loading is elevated near some landmasses (e.g., off Sahara, Saudi Arabia, India, and Southeast Asia) and in some open ocean regions [e.g., intertropical convergence zone (ITCZ) and the stormy “40°S” zonal belt]. It is unclear whether these latter features are “real” or indicative of retrieval problems, but in any case they are common to both products. Although the A product has more missing data compared to the M product, it extends farther south than the M product, while the opposite is true in the Northern Hemisphere. These features are mainly a consequence of excluding the solar side of the orbit in the A product.

In Figs. 2a(2) and 2b(2), based on MA intersection data, the differences between the τ_{1M} and τ_{1A} are mainly (yet not solely) due to the differences in the multichannel MOD04 and single-channel A-product algorithms. The two products are highly correlated. For example, for FM1, the linear correlation coefficient, R , equals 0.84 and 0.78 in December 2000 and June 2001, respectively. The differences between the two datasets are smaller than those for the full M and A products in Figs. 2a(1) and 2b(1), implying that the effect of the aerosol algorithm is less important than the effect of sampling. Another interesting feature is that τ_{1M} in the MA intersection is generally smaller than in its full product counterpart, whereas τ_{1A} is comparable in both cases. This suggests that τ_{1M} is larger in the M complement than it is in the intersection sample.

This is directly confirmed in Figs. 2a(3) and 2b(3) produced from the M and A complements. The τ_{1M} in the M complement is clearly larger than the optical depths in both the MA intersection and the M product. The difference is less pronounced in the A complement, which consists of only ~10% of the union sample and, therefore, has many data gaps. [Note that, although the maps in Figs. 2a(3) and 2b(3) were produced from nonoverlapping CERES footprints, there may be overlap due to averaging of individual CERES footprints within $7 \text{ day} \times (1^\circ)^2$ grids.]

Figure 3 shows plots of the global distribution of τ_2 . The Saharan dust region, dominated by large particles, is clearly evident, whereas smoke plumes with small particles around India, Saudi Arabia, and Southeast Asia are not as prominent as in Fig. 2. The τ_2 results have many points in common with the τ_1 results: 1) differences between the three subsamples in the M product are significant, whereas the A product is more uniform across all three subsamples, and 2) the M and A products are most consistent in the MA intersection (for τ_{2M} and τ_{2A} , $R = 0.61$ and 0.68 in December 2000 and June 2001, respectively). In both products, orbital striping seems to emerge more clearly in τ_2 compared to the τ_1 image.

The global distribution of the Ångström exponent

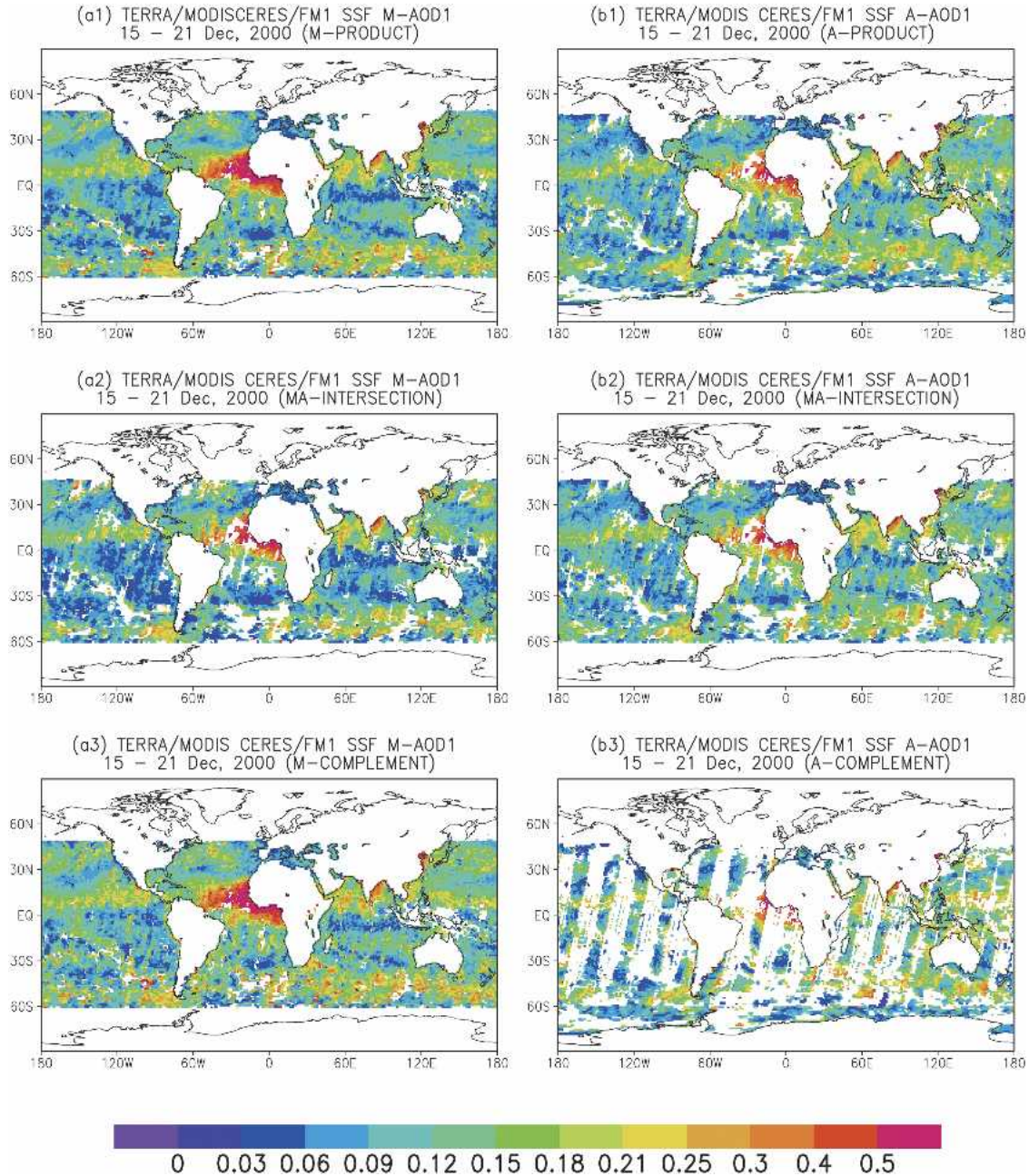


FIG. 2. (left) Mapping τ_{IM} (right) and τ_{IA} products for different subsamples (data of *Terra* CERES SSF FM1, Dec 2000): (a1), (b1) full product [$M \equiv (M \otimes A) \oplus (M \ominus A)$, $A \equiv (M \ominus A) \oplus (A \otimes M)$]; (a2), (b2) MA intersection ($M \otimes A$); (a3), (b3) M and A supplements [$(M \ominus A)$ and $(A \ominus M)$].

(α) from the M and A products is shown in Fig. 4. Observations 1 and 2 above for the τ maps also apply to α . The correlation between the α fields in the MA intersection is weaker compared to the τ fields ($R = 0.57$ and 0.38 in December 2000 and June 2001, respectively). This is due to the high sensitivity of the aerosol size parameter to τ errors, especially at low aerosol loadings over ocean (Ignatov et al. 1998; Ignatov 2002; Ignatov and Stowe 2002b). Orbital stripes are clearly

traced in both α_M and α_A retrievals. South of 60°S , α_M retrievals are not available and α_A data are clearly in error.

c. M- and A-aerosol retrievals: Global statistics

Figure 5 summarizes the average statistics of the M and A τ/α for December 2000 and June 2001 for FM1 and FM2. For each dataset, we provide two A statistics, based on panels b(2) and b(3) in Figs. 2–4, and two M

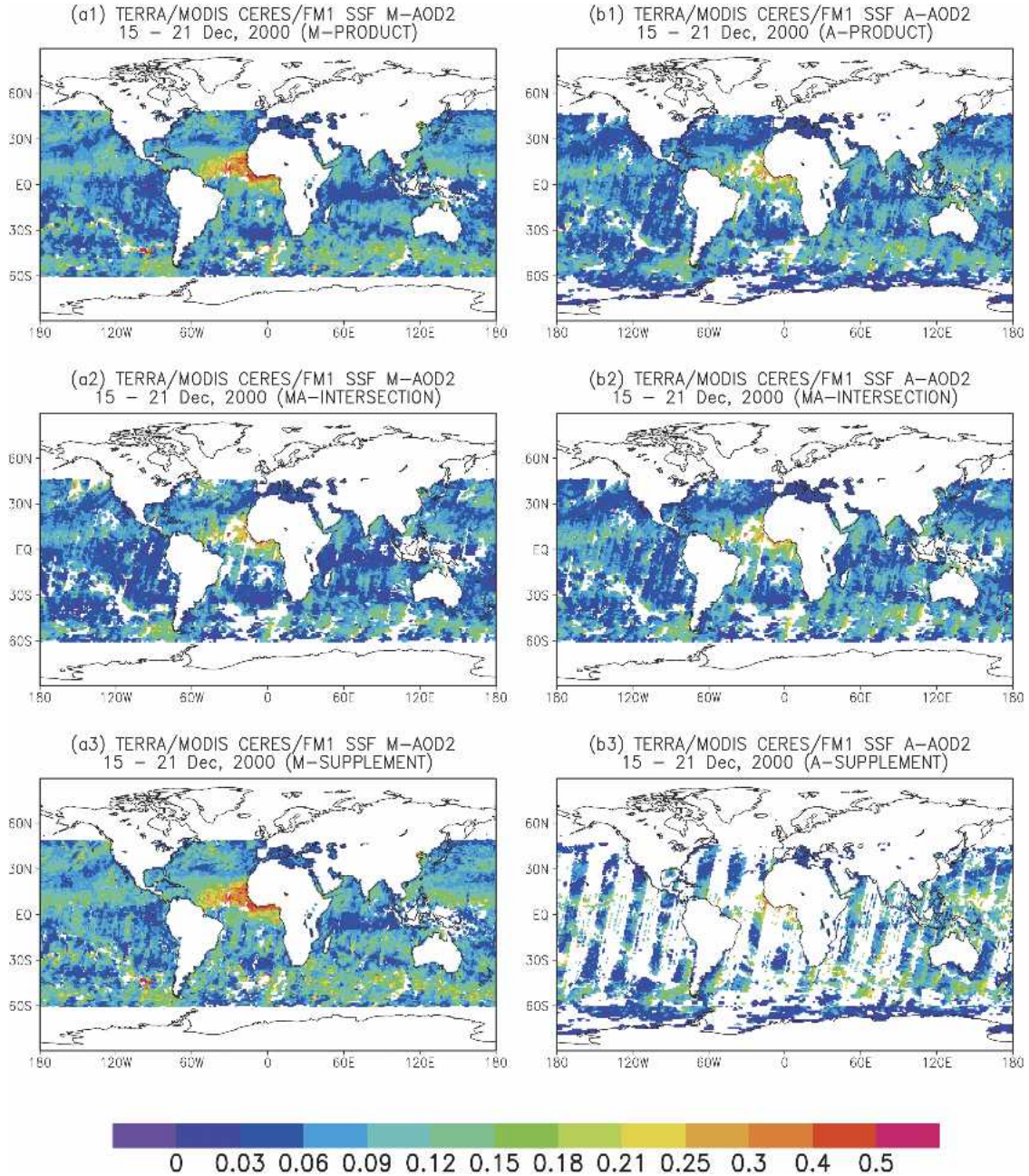


FIG. 3. As in Fig. 2 but for τ_2 .

statistics based on panels a(2) and a(3) in Figs. 2–4. Statistics for the M and A products in a(1) and b(1) in Figs. 2–4 fall between their intersection and complement counterparts and therefore are not shown here.

The following observations emerge from Fig. 5:

- (a) The M complement (cluster “4”) clearly stands out as different from the MA intersection (cluster “3”). The only difference between clusters 4 and 3 is sampling, as the M-aerosol algorithm is the same here.
- (b) Sampling-induced differences in the A product (be-

- tween the MA intersection and the A complement; clusters “1” and “2”) are generally smaller than the sample-induced M differences. The only exception is the α_A statistics in cluster 1 for June 2001, where the A complement is very small and its statistics are not globally representative (see analyses in section 3d and Fig. 6).
- (c) AOD is lower in June 2001 compared to December 2000. This difference is statistically significant in both bands 1 and 6, in both SSF datasets (FM1 and FM2), and in both products (M and A).

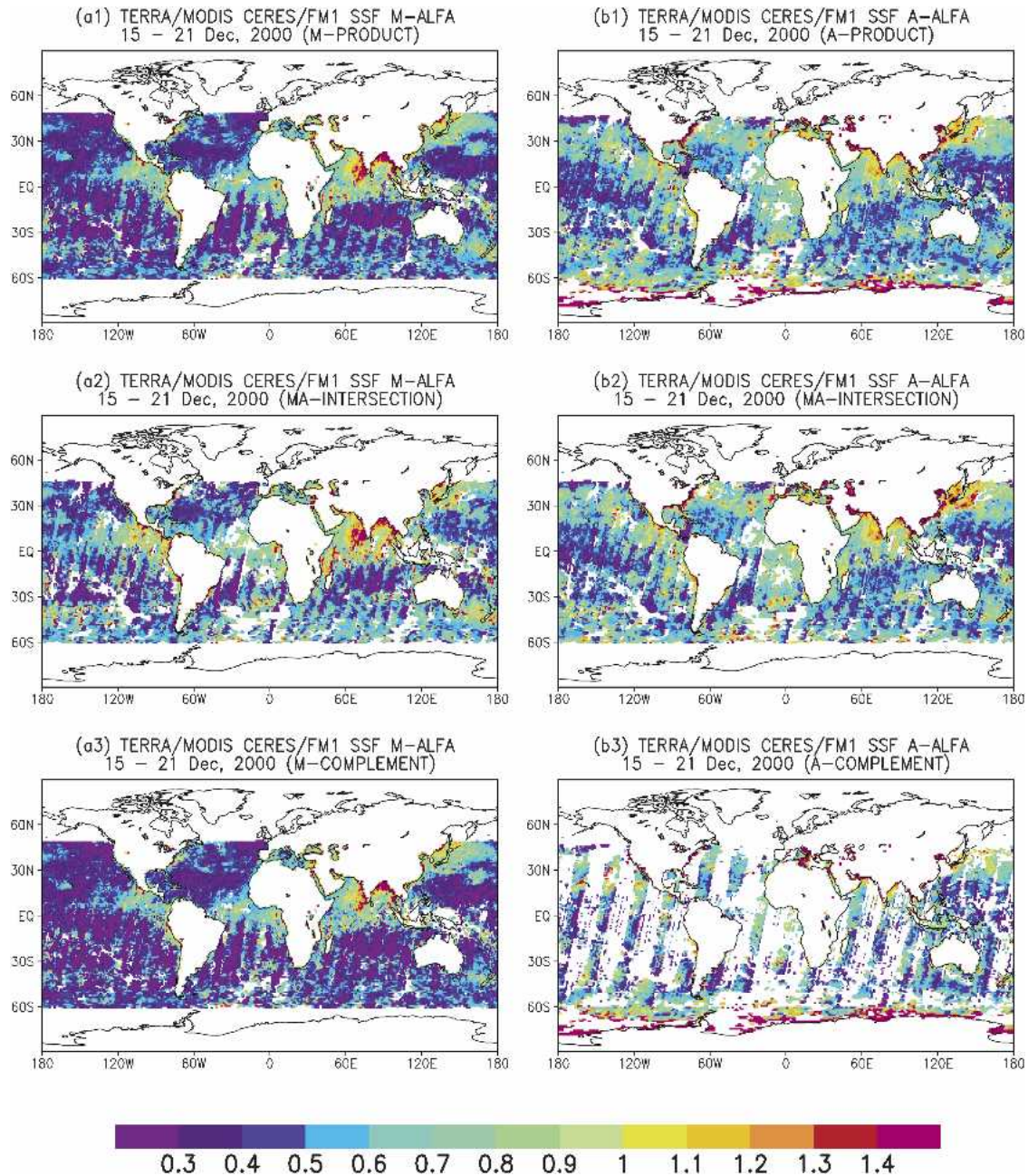


FIG. 4. As in Fig. 2 but for α .

- (d) Aerosol algorithm-induced global differences between the M and A retrievals in the MA intersection (cluster 2 versus 3) are within $\sim(4 \pm 5) \times 10^{-3}$ for τ_1 ; within $\sim(3 \pm 1) \times 10^{-3}$ for τ_2 , and within $\sim(1 \pm 1) \times 10^{-1}$ for α .
- (e) The FM2 τ statistics are somewhat higher compared to their FM1 counterparts. The cause for this difference is not entirely clear, but is likely related to sampling as opposed to aerosol algorithm differences.

d. Possible causes for the sampling M differences

To help determine if the M sampling differences between clusters 3 and 4 are due to geographical differences, Fig. 6 shows the average latitude and longitude statistics for the four datasets (note that the statistics are identical for clusters 2 and 3, which represent different aerosol retrievals in the same MA intersection domain). The latitude–longitude statistics of the M complement (cluster 4) and MA intersection (cluster 3)

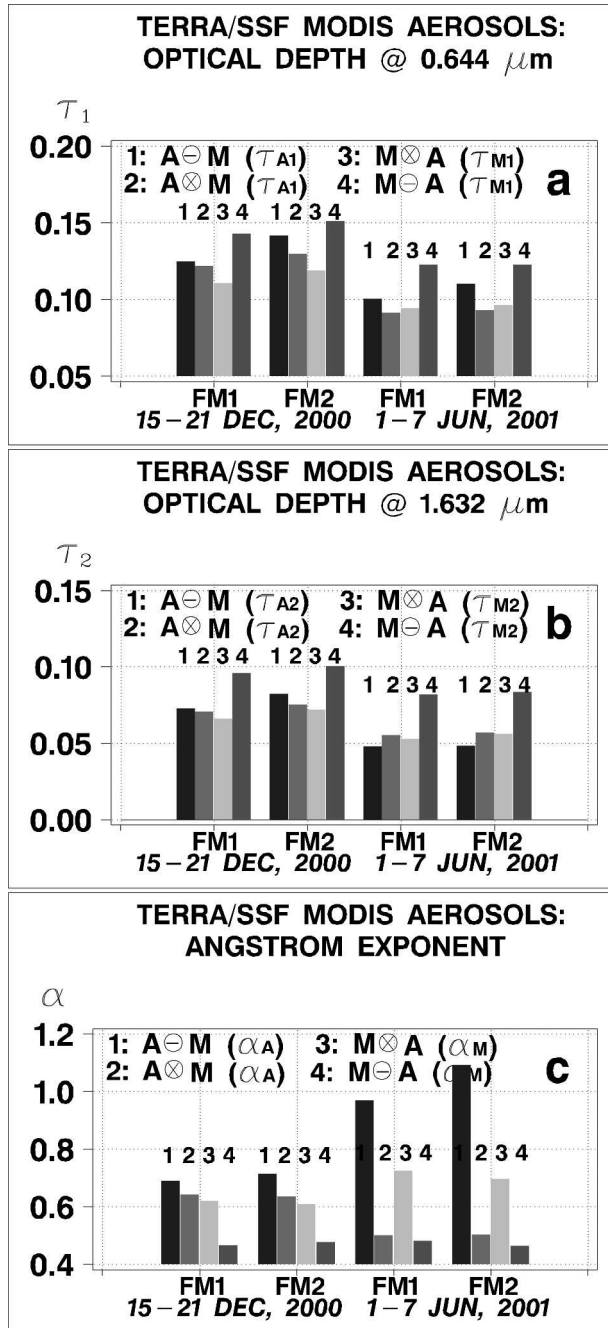


FIG. 5. Average statistics of aerosol retrievals in Dec 2000 and Jun 2001, FM1 and FM2 datasets. (Samples are defined in caption to Fig. 1.)

are very close, so geographical differences likely are not the reason for the observed differences. On the other hand, the A complement (cluster 1) is displaced from cluster 2 (especially in June 2001), which may explain the α_A anomaly in the A complement in June 2001 in Fig. 5.

Figure 7 shows histograms of the six other factors associated with the retrievals: cloud amount in the vi-

cinity of the aerosol retrievals, and five angles. Again, all statistics in clusters 2 and 3 are identical. Three clusters, 1–3, form a more or less uniform group, whereas the M supplement (cluster 4) clearly stands out in the average cloud amount, relative azimuth, and scattering angle histograms.

- 1) Cloud amount is $A_T \sim 39\%$ in clusters 1–3, whereas it is 59% in cluster 4. It should be noted that the A_T is a conditional estimate (i.e., only those CERES footprints were used with at least one aerosol retrieval), and that cloud amounts used here come from the A product.
- 2) Relative azimuth angle is $\sim 125^\circ$ in clusters 1–3 compared to $\sim 86^\circ$ in cluster 4. The relative azimuth cannot be less than 90° in the A retrievals, which are not produced on the solar side of the orbit, but it may be less than 90° in the M retrievals.
- 3) Scattering angle is $\sim 142^\circ$ in clusters 1–3 versus $\sim 120^\circ$ in cluster 4.

Understanding the mechanisms of how factors 1–3 may affect the aerosol retrievals is the subject of future research (note also that some factors may be interdependent or cross correlated, e.g., the relative azimuth and scattering angles).

e. Possible causes for the December 2000–June 2001 aerosol differences

Figure 8 provides τ_M versus τ_A and α_M versus α_A for June 2001, in the MA intersection. These are compared with the corresponding December 2000 results in Figs. 2–4. The AODs in June 2001 are lower than in December 2000 in both bands. The difference is most prominent in the cleanest remote areas of the Southern Hemisphere and over the central Indian and Pacific Oceans. Figure 8 confirms that the global aerosol statistics change significantly over the 5½-month period. This change is observed in both aerosol products and far exceeds the differences between the M and A products in any given month. For instance, the average τ_1 is ~ 0.11 in December 2000 compared to $\tau_1 \sim 0.09$ in June 2001. A similar change is observed in τ_2 . Figures 6 and 7 suggest that these differences are not likely to be related to differences in geography, cloud amount, or viewing geometry. Figure 5 also shows that the Angstrom exponents change in a more complicated way from December 2000 to June 2001. In the MA intersection, α_M increases from ~ 0.6 to ~ 0.7 , whereas α_A decreases from ~ 0.6 to ~ 0.5 . This is consistent with the comparisons in Figs. 8 and 4a(2), b(2).

The sensor radiometric performance is one possible cause for the observed aerosol changes. The MODIS underwent a number of changes and experienced some short interruptions due to instrument problems early in Terra operations after science data collection began 24 February 2000. The MODIS A-side electronics (“A-I”) was used from 24 February to 26 October 2000. On 30

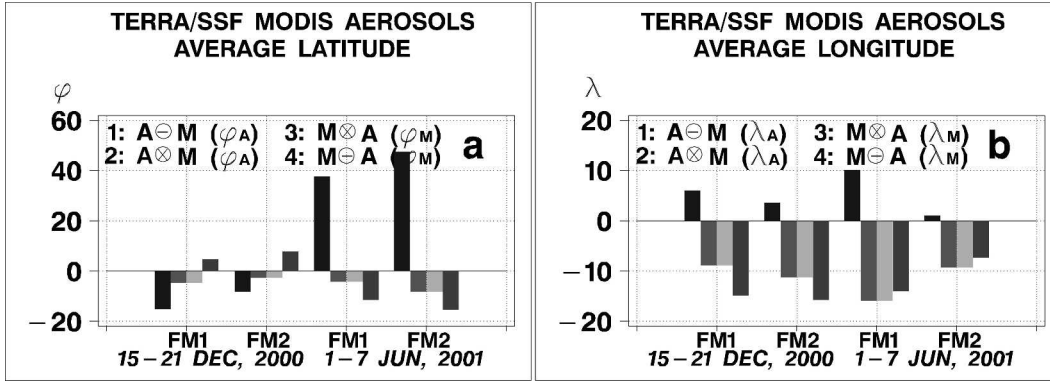


FIG. 6. Average latitude and longitude in Dec 2000 and Jun 2001, FM1 and FM2 datasets. (Samples defined in caption to Fig. 1.)

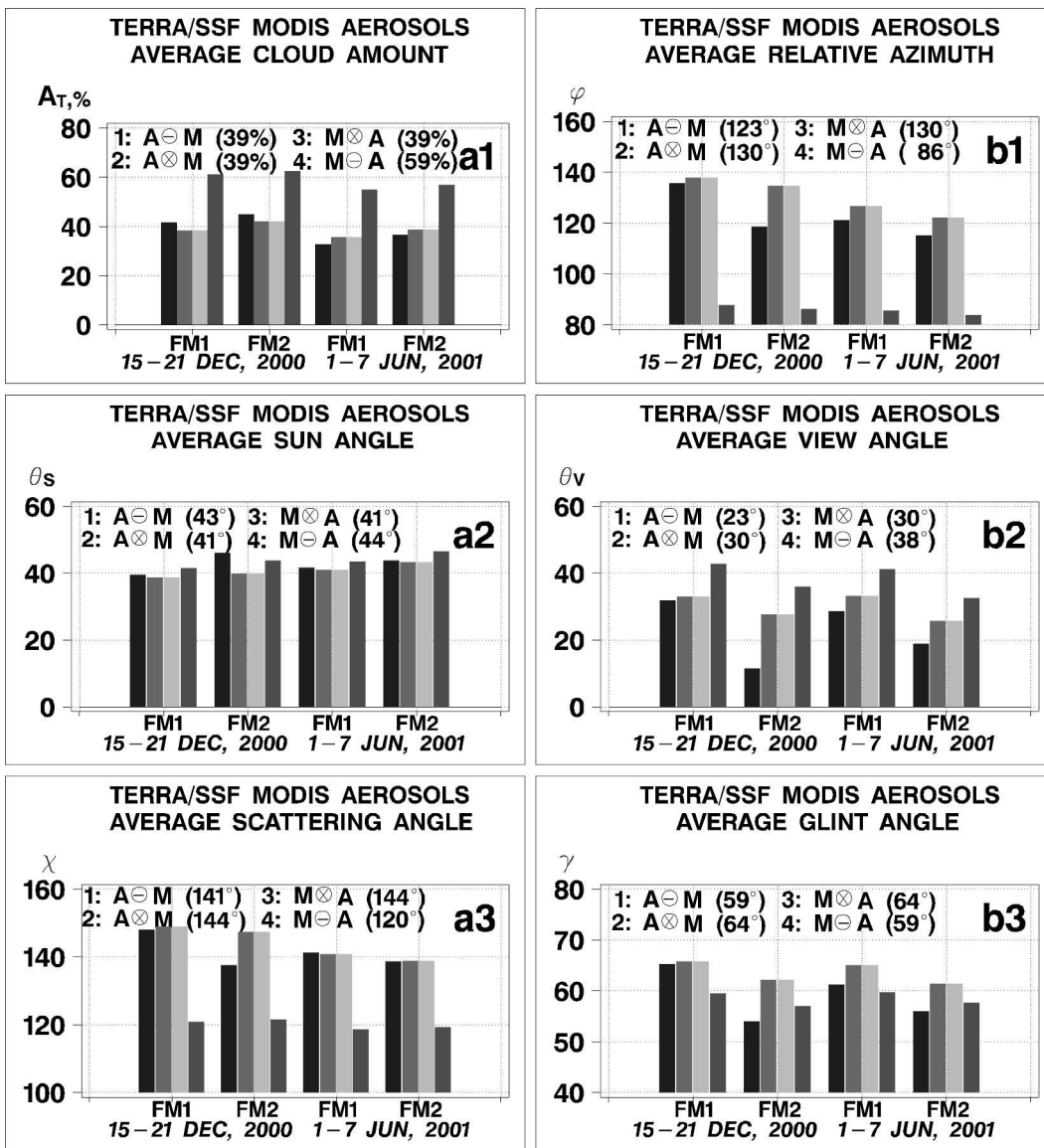


FIG. 7. As in Fig. 6 but for (a1) ambient cloud amount; (b1) relative azimuth angle; (a2) solar zenith angle; (b2) view zenith angle; (a3) scattering angle; and (b3) glint angle.

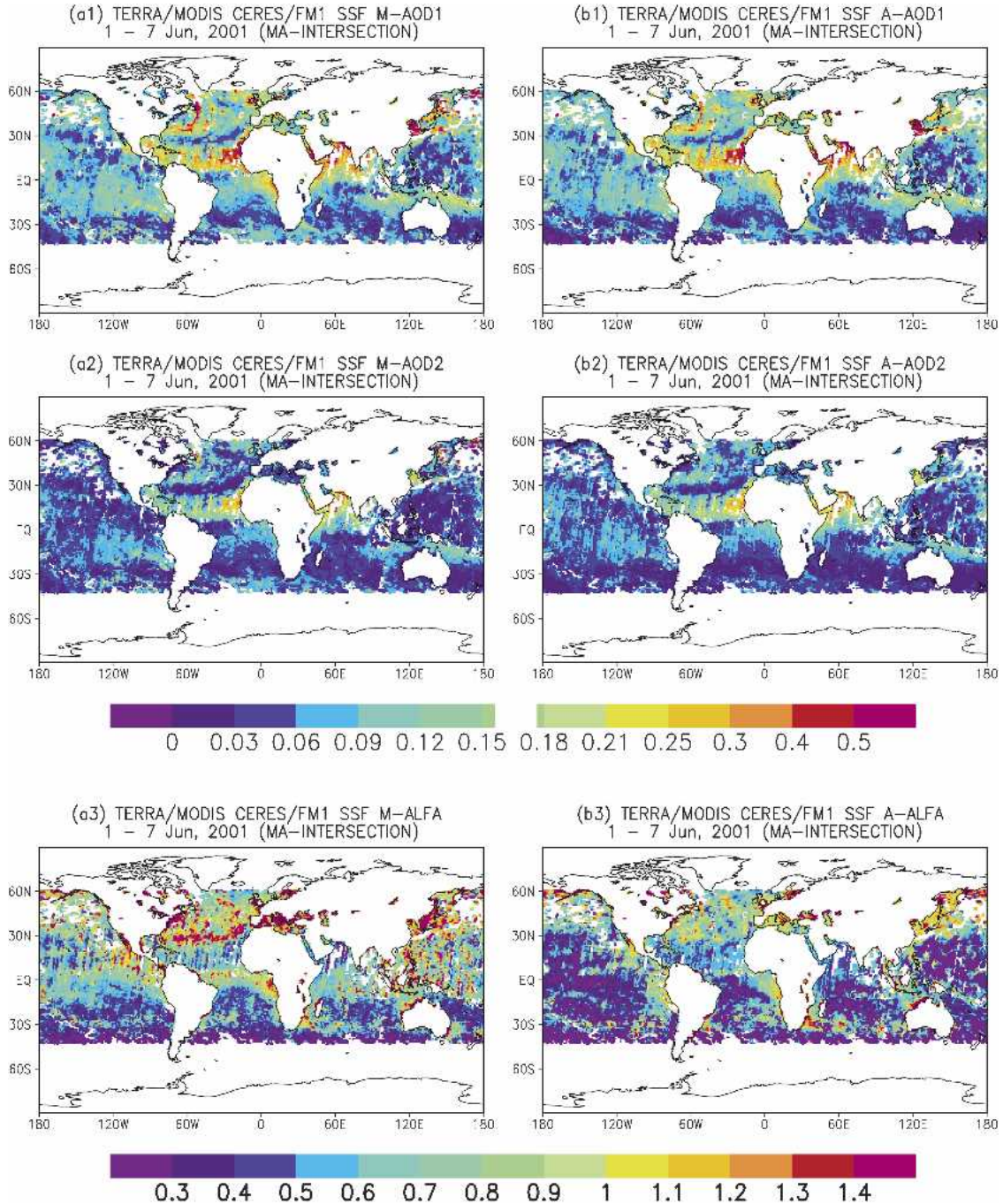


FIG. 8. Distribution in MA intersection of [a(1), b(1)] τ_1 , [a(2), b(2)] τ_2 , and [a(3), b(3)] α derived from *Terra* CERES/FM1 SSF in Jun 2001: (left) M product and (right) A product. Compare with distributions in the MA intersection in Dec 2000: τ_1 in Figs. 2a(2)–b(2); τ_2 in Figs. 3a(2)–b(2); and α in Figs. 4a(2)–b(2). (See discussion in section 3e.)

October 2000, the B-side electronics (“B”) was enabled and used until 15 June 2001. After experiencing a power supply 2 (PS-2) shutdown anomaly, the MODIS used the power supply 1 (PS-1) and the A-side electronics (“A-II”). According to the MODIS Characterization Support Team (MCST), the MODIS instrument

has performed as expected after the last switch (see appendix A for definitions and more detail).

The two datasets analyzed in this study, in December 2000 and June 2001, both belong to the same B electronics/PS-2 period of MODIS life cycle, during which the measurement quality improved dramatically ac-

according to the MCST. However it is possible that some subtle radiometric changes continued to occur during this “stable” period, especially shortly before and after the switches. Aerosol is known to be a very sensitive indicator of sensor radiometric uncertainties (Ignatov 2002, 2003; Ignatov and Stowe 2002b; Ignatov et al. 2004), but the M and A products may respond to calibration errors differently. The M product weighs all bands together in a complicated way. Its sensitivity to (random in bands) calibration errors has been documented by Tanré et al. (1997), but the instrument switches may not be random from band to band as they affect all bands coherently. For example, it has been observed that each switch affected the aerosol size parameter estimated from MODIS (REM). On the other hand, the single-channel A algorithm emphasizes the information content of each individual band. Thus the opposite trends in the M and A Ångström exponents may be related to a different reaction of the M- or A-product algorithms to radiometric perturbations in different MODIS bands. More analyses are needed to understand the observed change of aerosol parameters with time.

f. Differences due to aerosol algorithm: Focus on the MA intersection

Examination of the effect of M-aerosol and A-aerosol algorithm differences is best achieved by using the MA intersection where the effect of sampling is minimized though not removed completely, as different MODIS pixels within a CERES FOV could have been used by each algorithm. The respective A – M differences are mapped in Fig. 9. The τ differences, which reach a few hundredths of τ , appear to increase with solar zenith angle and vary with scan position. More analyses are needed to determine if the M, A, or both products are responsible for the patterns. These artifacts may also be related to the aforementioned residual sampling differences. For example, Guzzi et al. (1998) indicate that residual cloud in a sensor FOV may cause artificial sun-angle trends in the retrieved AOD.

In December 2000 (Fig. 9, left), the biases in τ appear to be quasi *multiplicative* in both bands, suggesting that they mainly originate from differences between the M- and A-aerosol models (e.g., Ignatov and Stowe 2002a) and largely cancel out when their ratio is used to calculate the Ångström exponent. In June 2001, the $\tau_A - \tau_M$ differences are smaller, but there is no cancellation in calculating α , indicating the presence of *additive* errors in either τ_A or τ_M , or both. According to Ignatov (2002), additive errors may be caused by calibration slope uncertainties. As a result, the $(\alpha_A - \alpha_M)$ differences in June 2001 show large spatial variability, with an overall negative bias of ~ -0.2 . The global α statistics in Fig. 5 are in quantitative agreement with this visual estimate from Fig. 9.

g. Cloud amount trends in aerosol retrievals

The cloud–aerosol correlations in the M and A products are examined to explore the possibility that the aerosol sampling biases found in section 3d are caused by cloud contamination. The top panels of Fig. 10 show histograms of A_T for December 2000 and June 2001. In both products, the cloud amount is more or less uniformly distributed in the $\sim 0\%$ – 80% range. Intuitively, a progressively smaller proportion of aerosol observations is expected at high ambient cloud cover. This is indeed the case in the A product (at $A_T > 80\%$), whereas the increasing trend in the M product is unexpected.

Figures 10a(2)–a(4) and 10b(2)–b(4) show aerosol retrievals as a function of A_T . The trends in τ/α with A_T are strong in both the M and A products. Similar trends have been previously observed in the NOAA/AVHRR and TRMM/VIRS aerosol retrievals (Ignatov and Nalli 2002; Ignatov et al. 2005, unpublished manuscript). The A_T differences between the MA intersection ($A_T \sim 39\%$) and the M supplement [$A_T \sim 59\%$; cf. Fig. 7a(1)] combined with the results in Fig. 10 suggest that cloud-screening differences between the M and A products are the likely cause for the τ -retrieval differences observed in Fig. 5. The aerosol–cloud correlations are either “real” (increased hygroscopic aerosol particles that influence cloud formation) or artifacts of the retrievals (residual cloud in a MODIS field of view). The increased sensitivity in τ_M to A_T , as compared to sensitivity of τ_A to A_T , suggests that the residual cloud is definitely present and contributes to the observed trends. However the Ångström exponent trends in Figs. 10a(4) and 10b(4) are consistent with both hypotheses: $\alpha \sim 1$ when $A_T \sim 0\%$, decreases to $\alpha \sim 0.5$ at $A_T \sim 20\%$ – 40% , and flattens thereafter. (Note that the α_A shows some residual artifacts at large A_T that are not fully understood.) Further studies are needed to explain these features.

Figure 10 also reveals significant differences between December 2000 and June 2001. In band 1, the minimum in τ_A is ~ -0.04 in December 2000 and decreases to ~ -0.07 in June 2001. Negative values of τ are possible in the A product, whereas the M product truncates negative retrievals. The seasonal shift in the τ_A minimum is consistent with the shift in the mean values of τ_A in Fig. 5. If this difference was caused by a calibration slope change, it would be equivalent to an $\sim 3\%$ – 4% degradation over 5 months of *Terra* operation (Ignatov 2002). Change in calibration intercept may also contribute to the observed decline in (τ) . In band 6, the minimum τ_{2A} is slightly negative but close to zero due to truncation of negative radiances (see appendix A and Fig. A2).

4. Discussion and conclusions

Two aerosol products over oceans available on the *Terra* and *Aqua* CERES SSF datasets reveal common

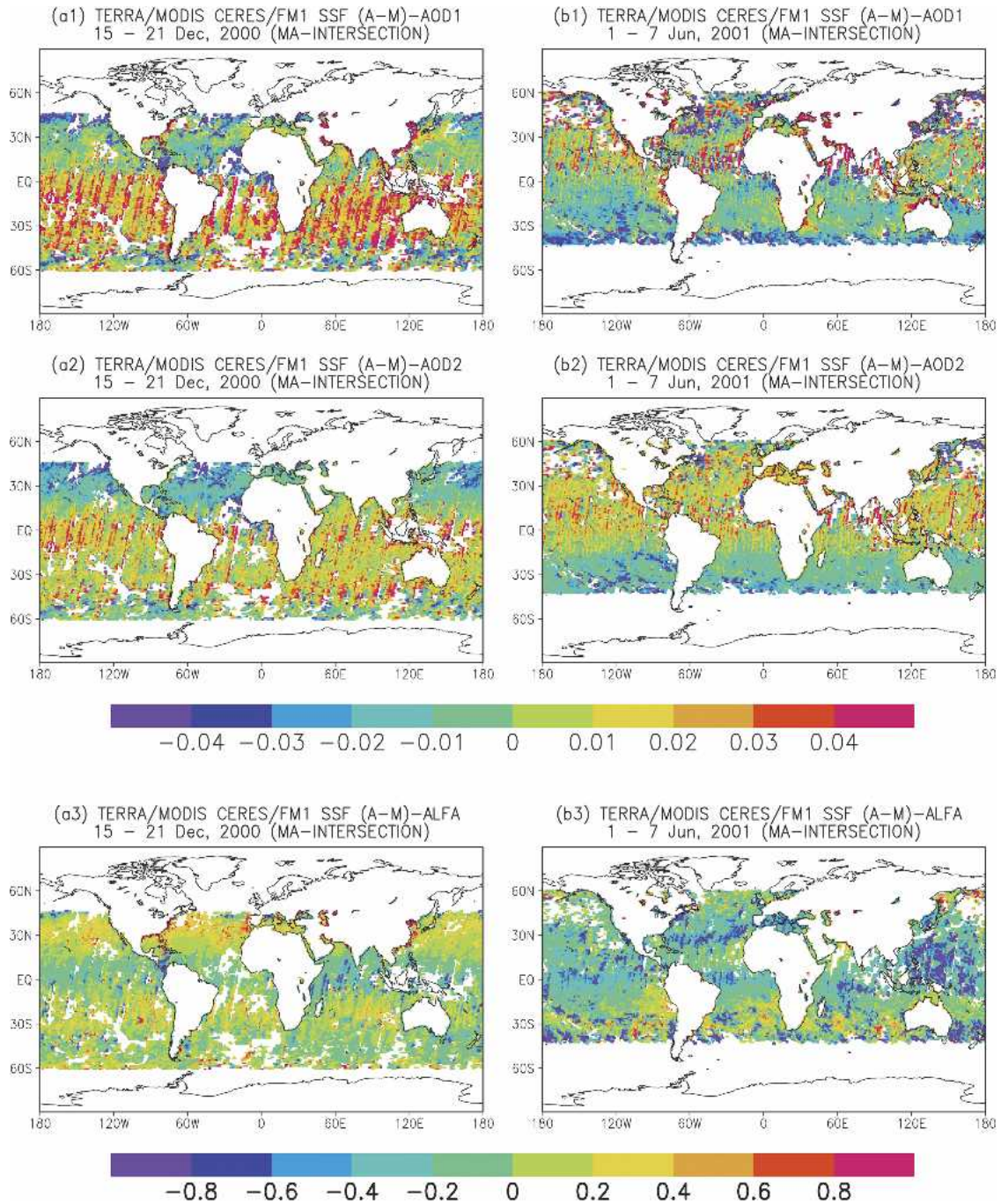


FIG. 9. Distribution in MA intersection of [a(1), b(1)] $\tau_{1A}-\tau_{1M}$; [a(2), b(2)] $\tau_{2A}-\tau_{2M}$; and [a(3), b(3)] $\alpha_A-\alpha_M$ derived from *Terra* CERES/FM1 SSF in (left) Dec 2000 and (right) Jun 2001. (See discussion in section 3f.)

features and some differences due to different sampling and aerosol algorithms.

The M- and A-product aerosol algorithms differ significantly. The globally invariant aerosol model in the A product is clearly a limitation, which is purportedly alleviated in the M product. Note also that there are many nonaerosol factors in the aerosol algorithms

(such as the ocean surface reflectance, Rayleigh scattering, gaseous absorption, RTM, and numerical inversion) that are treated differently. Their cumulative result can be assessed only through empirical analyses. The MA intersection sample constructed in this study is best suited to highlight the aerosol algorithm differences. The comparisons demonstrate that aerosol algo-

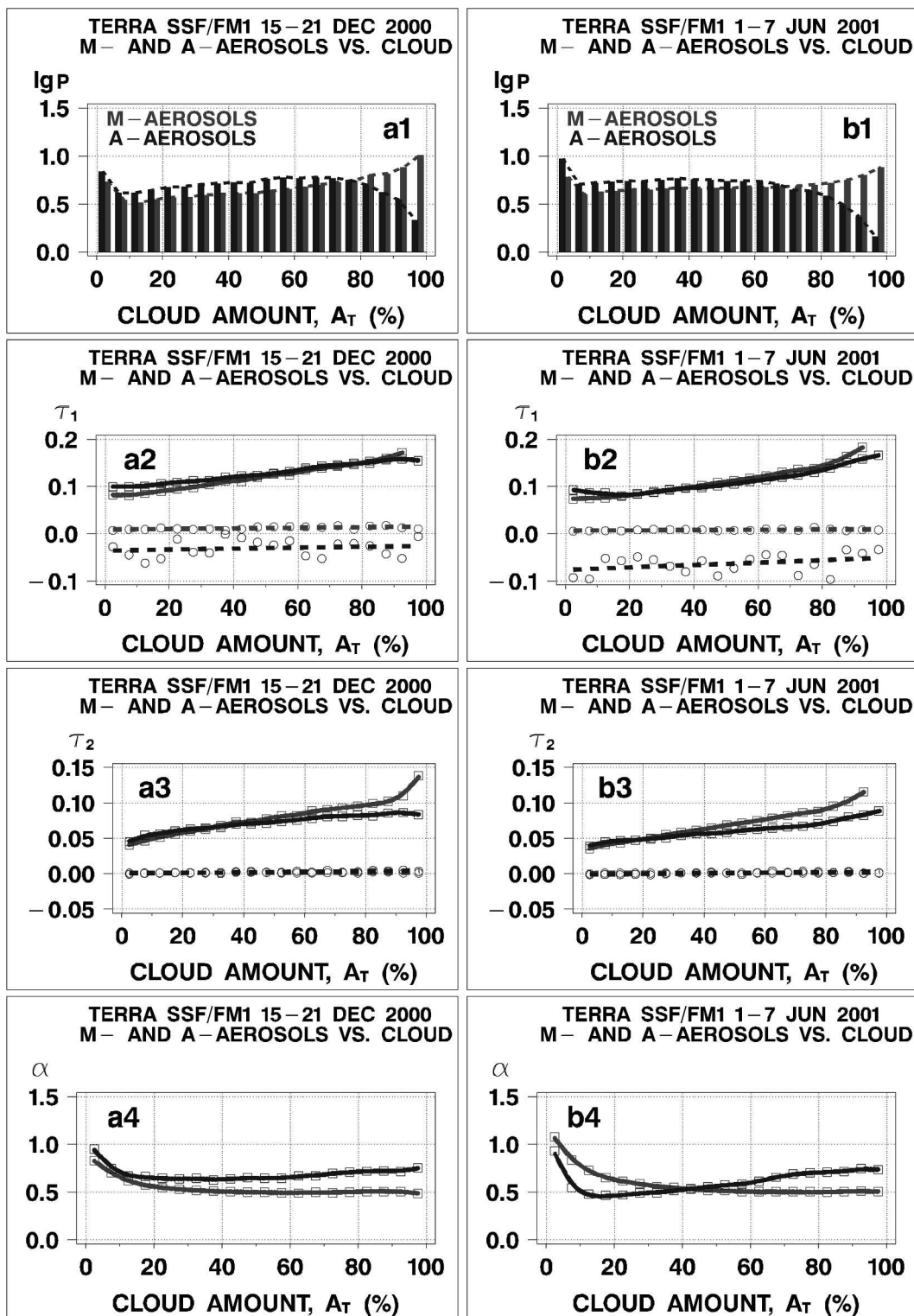


FIG. 10. [a(1), b(1)] Histograms of cloud amount, A_T ($\Delta A_T = 5\%$), and [a(2)–b(4)] aerosol retrieval trends for (left) Dec 2000 and (right) Jun 2001 datasets. (See discussion in section 3g).

rithm-induced global differences between the M and A retrievals are within $\sim(4 \pm 5) \times 10^{-3}$ for τ_1 , $\sim(3 \pm 1) \times 10^{-3}$ for τ_2 , and $\sim(1 \pm 1) \times 10^{-1}$ for α . The $\tau_M - \tau_A$ differences appear to be sun angle and scan position dependent, and may reach +0.04 in certain domains of sun-view geometries. Some residual sampling discrepancies may still contribute to the observed differences. The aerosol algorithm differences are currently being analyzed in depth, and the results will be reported elsewhere.

However, most of the discrepancy between the two products is due to different sampling. The M products are available in $\sim 90\%$ of the union MA sample, whereas the A products occur in only $\sim 55\%$. Aerosol statistics in the M supplement (M product only) differs from the MA intersection sample by $\sim+(0.030 \pm 0.003)$ for both τ_1 and τ_2 , and by $\sim-(0.20 \pm 0.05)$ for α . The A-product differences between the A supplement and MA intersection are statistically insignificant. A possible explanation is related to the fact that aerosol retrievals strongly correlate with the ambient cloud amount in both products, although the dependence on cloud amount in the M product is more pronounced than in the A product. Similar cloud-aerosol correlations have been observed previously in the NOAA/AVHRR and TRMM/VIRS aerosol retrievals. Drawing a line between the cloud and aerosol is ambiguous. Selecting the thresholds in the cloud screening algorithms is not a completely objective procedure. Note that Myhre et al. (2004) compared five different aerosol products derived from four satellite sensors on three platforms and concluded that the major cause for the observed aerosol differences are likely due to the differences in cloud screening. Further study is needed to resolve these issues. Other reasons for differences between the two aerosol products are likely related to a different domain of scattering and/or relative azimuth geometries for the samples remaining after cloud and glint screening.

Comparison of the global December 2000 and June 2001 statistics indicate a systematic decrease in aerosol optical depths over the 5½-month period in both products. The two-band τ analyzed in this study (0.644 and 1.632 μm) change in the same direction but not exactly coherently, leading to opposite trends in the Ångström exponents in the two products: the α_M increases by $\sim +0.1$ whereas the α_A decreases by ~ -0.1 . Neither of these changes is associated with a significant shift in the geographic or angle domain or in the cloud amount. Seasonal change, if extant, would be minimal in the most pristine ocean areas and therefore is unlikely to affect the minimum in τ . However, the band-1 A product clearly shows a decline of ~ 0.03 in the τ minimum from December 2000 to June 2001. An analysis of band-6 minima is impossible due to radiance truncation. A possible explanation for the change in the minima is the variation in the MODIS performance, which affects the multichannel M and the single-

channel A products differently. This example highlights the need for a continuous in-flight monitoring of the performance of all *individual bands* of both MODIS instruments. This should be done as a part of an aerosol quality assurance process as an addition to the MODIS Characterization Support Team tests.

Aerosol retrievals are obtained from the lowest observed radiances and thus are very sensitive to even the smallest radiometric uncertainties and residual errors of cloud and glint screening. Including single-channel A-type retrievals from each MODIS band used in the standard MOD04 processing would provide an excellent indicator of overall band performance from an aerosol user perspective. Such work should also be closely coordinated with the ocean color retrievals, which are known to be even more demanding to the input data accuracy (G. Feldman and C. McClain 2004, personal communication). We also recommend an end to the current double truncation of negative radiances on the level 1B processing and negative aerosol optical depths in the MOD04 processing. Regular (at least one orbit per day) collection of data in the solar reflectance bands on the dark side of the earth would help to monitor the radiometric performance of the solar reflectance bands (Ignatov 2003). These steps could improve the ability to monitor/diagnose the actual performance of the MODIS instrument in-flight and greatly facilitate correcting any problems. As an improvement to the current CERES SSF processing, saving six MODIS radiances used for the MOD04 retrievals over oceans (which are available on MOD04 product) on the SSF datasets would greatly benefit their utility for aerosol analyses and improvements.

The exact comparison numbers may be refined in the future, as newer collections of MOD04 products (004 and 005) become available, and the A processing undergoes some changes (such as, i.e., change in sampling from every second line/second pixel to every second line/fourth pixel). Nevertheless, these initial comparisons of the two MODIS-based marine aerosol products indicate that the more spectrally complex MOD04 and simpler AVHRR-type aerosol methods produce relatively consistent results. Although further detailed analyses of the datasets used here and later retrievals will provide information necessary to fully reconcile the discrepancies, it appears that a reliable linkage can be established between the older record based on the simpler methods and the current and future retrievals using more sophisticated approaches. With that connection, it will be possible to establish a trustworthy and valuable long-term climatology of oceanic aerosol properties.

Acknowledgments. The MOD04 algorithms were developed in late 1990s by the international team of scientists (NASA GSFC, United States, and Laboratoire d'Optique Atmosphérique, University of Lille, France) under energetic and enthusiastic leadership of Yoram Kaufman. The A-product retrievals were initiated in

late 1980s by Nagaraja Rao (deceased) and Larry Stowe (retired) at NOAA/NESDIS following the pioneering ideas by Michael Griggs proposed in mid-1970s. The A product has been enhanced and applied to other sensor data (TRMM VIRS, and *Terra/Aqua* MODIS) under the CERES project. The authors are indebted to Jack Xiong, Bill Barnes, Bruce Guenther (NASA GSFC-MCST), Chris Moeller (University of Wisconsin—Madison), Kurt Thome (The University of Arizona), and Chagyong Cao and Jerry Sullivan (NOAA/NESDIS) for helpful discussions of the MODIS radiometric issues. Help and advice from Richard Hucek, Shana Mattoo, Allen Chu, Rob Levy, Rong-Rong Li, Vincent Chiang, and Gwyn Fireman (NASA GSFC), and Qing Trepte and Robert Arduini (NASA LaRC) is also appreciated. This work was funded under the NASA EOS/CERES (NASA Contract L-90987C), the Integrated Program Office (IPO/NOAA/NASA/DOD), NOAA Ocean Remote Sensing, and Joint Center for Satellite Data Assimilation (NOAA/NESDIS) Programs. We thank Steve Mango (IPO) and Bill Pichel and Fuzhong Weng (NOAA/NESDIS) for their support and encouragement. The *Terra* CERES SSF data used in this study were obtained from the Atmospheric Sciences Data Center at NASA Langley Research Center. Thoughtful and constructive reviews by Tom Charlock and Bill Smith Jr. (NASA LaRC), and by two anonymous reviewers were instrumental for improved style and clarity of presen-

tation. The views, opinions, and findings contained in this report are those of the authors and should not be construed as an official NOAA or U.S. Government position, policy, or decision.

APPENDIX A

MODIS Definitions

MODIS takes measurements in 36 spectral bands, of which 20 are solar reflectance bands (SRBs; see MCST 2002a,b; Xiong et al. 2002; and <http://www.mcst.ssai.biz/mcstweb/index.html>). MODIS level 1B data (termed MOD02 and MYD02 for *Terra* and *Aqua*, respectively) are available in three spatial resolutions: 250 m in bands 1–2 [Q(quarter) km]; 500 m in bands 1–7 [H(alf) km; in bands 1–2, 2×2 pixels are aggregated]; and 1000 m in all bands [1 km; in bands 1–2 and 3–7, 4×4 and 2×2 pixel averaging is done].

Each band is characterized by a finite relative spectral response (RSR; Fig. A1). Higher spatial resolution in aerosol bands (250/500 m in bands 1–2/3–7; 1000 m in all other bands) is achieved through the use of 40/20 detectors per band, respectively. All RSRs are supposed to be the same for all detectors within a band and for similar bands of the two instruments but, in fact, they slightly vary, as shown in Fig. A1. The “effective” wavelength, λ_{eff} , is customarily used to identify a band’s spectral position. The definition of λ_{eff} may be not

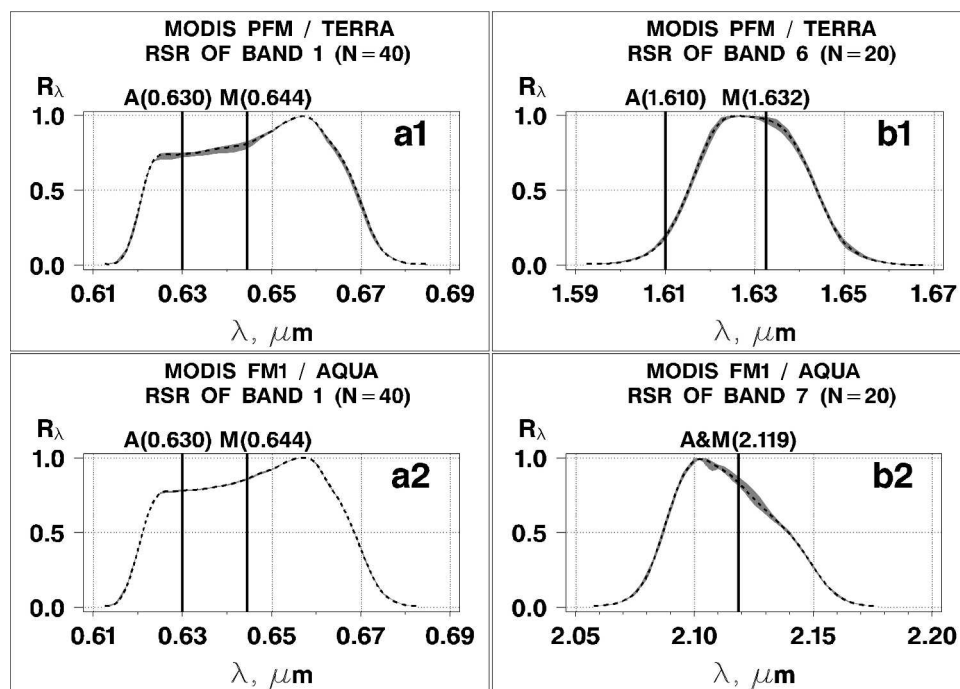


FIG. A1. RSR of the MODIS bands used in the AVHRR-like retrievals (a) 1 and (b) 6(7) on (top) *Terra* and (bottom) *Aqua*. Superimposed are reference wavelengths at which the A and M products are reported. (Solid lines represent average RSRs over the 40/20 detectors, and shaded areas show cross-detector variability.)

TABLE A1. Effective central wavelengths λ_{eff} (nm) for seven MODIS bands used in M-aerosol retrievals over ocean. Values of λ_{eff} (bands 1–3) cited in literature and (bands 4–5) calculated in this study according to Ignatov and Stowe (2002a) for MODIS PFM (*Terra*) and FM1 (*Aqua*) filters (available online at <http://www.mcst.ssai.biz/mcstweb/info/faq.html>). Values by REM are used throughout this work.

Band (No. of detectors)	Reference			Current work	
	1) Xiong et al. (2002)	2) Tanré et al. (1997)	3) REM	4) <i>Terra</i> Mean (std dev)	5) <i>Aqua</i> Mean (std dev)
1 ($N = 40$)	645	659	644	645.8 (0.011)	645.3 (0.002)
2 ($N = 40$)	858	865	855	856.2 (0.012)	856.6 (0.009)
3* ($N = 20$)	469*	470*	466*	465.7* (0.007)	466.0* (0.002)
4 ($N = 20$)	555	555	553	553.7 (0.004)	553.9 (0.002)
5 ($N = 20$)	1240	1240	1243	1242.0 (0.032)	1241.3 (0.014)
6 ($N = 20$)	1640	1640	1632	1629.1 (0.030)	1627.9 (0.012)
7 ($N = 20$)	2130	2130	2119	2113.6 (0.019)	2113.4 (0.011)

* Band 3 on both platforms and band 6 on *Aqua* are not used. They are listed for reference only.

unique. Shown in Table A1 are different values of λ_{eff} cited in MODIS literature (columns 1–3) and our own calculations of λ_{eff} performed for this study (columns 4–5). The latter two columns report mean and standard deviation (std dev) statistics, over all 40/20 detectors, of λ_{eff} calculated by applying equations from Ignatov and Stowe (2002a) to the RSR of each individual detector. The small standard deviations indicate overall excellent reproducibility of the RSRs within a band: std dev (λ_{eff}) ≤ 0.03 nm for *Terra*, and ≤ 0.01 nm for *Aqua*. In this study, the λ_{eff} listed in column 3 after REM are used for consistency with the MODIS aerosol group who report their τ retrievals at these λ_{eff} .

MODIS L1B SRB data contain two standard products: the (earth-view overhead) reflectance, $\rho_{\text{EV}} \mu_o$ ($\mu_o \equiv \cos\theta_o$, θ_o is the solar zenith angle), and the (earth-view) radiance, L_{EV} (MCST 2000, 2002a,b; Xiong et al. 2002). Reflectance normalized at earth–sun (ES) distance of $d_{\text{ES}} = 1$ AU is the primary product, from which the spectral radiance, $L_{\text{EV},i}$ ($\text{W m}^{-2} \mu\text{m}^{-1} \text{sr}^{-1}$) (not normalized at $d_{\text{ES}} = 1$ AU) is derived as $F_{\text{eff},i} \rho_{\text{EV},i} \mu_o / d_{\text{ES}}^2$. Here, $F_{\text{eff},i}$ ($\text{W m}^{-2} \mu\text{m}^{-1} \text{sr}^{-1}$) is the solar spectral irradiance normalized with π and at $d_{\text{ES}} = 1$ AU. The values of F_{eff} for all bands and detectors are avail-

able from L1B files. Columns 1 and 3 of Table A2 list, by band, the mean and standard deviation of the individual-detector F_{eff} as read directly from the L1B data. Note that the L_{EV} product on L1B is estimated from the $\rho_{\text{EV}} \mu_o$ using the mean F_{eff} (MCST 2002b). For comparison, columns 2 and 4 of Table A2 list the mean/standard deviation statistics of our own calculations of F_{eff} following Ignatov and Stowe (2002a). In bands 1, 2, and 4 (from ~ 0.55 to $0.85 \mu\text{m}$), the two F_{eff} agree within a few tenths of a percent. For shorter (band 3) and longer (bands 5–7) wavelengths, the differences reach a few percent, possibly due to the uncertainties in the solar spectrum for narrow spectral intervals. These differences hint at possible errors and need further clarification. The MCST (2002) values are used in this study, for consistency with the mainstream GSFC processing. For reference, Table A3 summarizes our calculations of Rayleigh, τ^{R} , and gaseous, τ^{G} , optical depths in the seven MODIS SRBs for the six standard atmospheres. These data are referred to and discussed in the text.

Aerosol retrievals over ocean rely on the lowest TOA radiances, which are very challenging to measure accurately due to larger relative contributions from radiometric noise, digitization, and possible calibration

TABLE A2. Mean (std dev) statistics (over N detectors) of effective “solar constants,” F_{eff} ($\text{W m}^{-2} \text{sr}^{-1} \mu\text{m}^{-1}$), for the seven bands used in aerosol retrievals over ocean for MODIS (bands 1–2) PFM (*Terra*) and (bands 3–4) FM1 (*Aqua*). Data: (bands 1,3) derived from the “Solar Irradiance on RSB Detectors over pi” global attribute on MODIS L1B (MCST 2002b); (bands 2,4) calculated in current study according to Ignatov and Stowe (2002a). [Percent deviation from MCST (2002b) is also shown.] Values of F_{eff} listed on MODIS L1B (bands 1,3) are used throughout this work.

Band / λ_{eff} (No. of detectors)	MODIS PFM (<i>Terra</i>)		MODIS FM1 (<i>Aqua</i>)	
	1) MCST(2002b)	2) Current study	3) MCST (2002b)	4) Current study
1 / 644 nm ($N = 40$)	511.26 (0.607)	510.19/–0.21% (0.039)	511.86 (0.185)	510.74/–0.22% (0.008)
2 / 855 nm ($N = 40$)	315.83 (0.142)	316.20/+0.12% (0.040)	315.55 (0.118)	315.96/+0.13% (0.037)
3* / 466 nm ($N = 20$)	664.61* (0.032)	641.57/–3.47% (0.018)	664.69* (0.071)	641.57/–3.48% (0.046)
4 / 553 nm ($N = 20$)	593.95 (0.024)	592.22/–0.29% (0.005)	593.74 (0.050)	592.16/–0.27% (0.017)
5 / 1243 nm ($N = 20$)	150.99 (0.016)	145.59/–3.58% (0.015)	151.18 (0.006)	145.92/–3.48% (0.006)
6 / 1632 nm ($N = 20$)	76.47 (0.015)	75.49/–1.28% (0.005)	76.59 (0.013)	75.67/–1.20% (0.001)
7 / 2119 nm ($N = 20$)	28.75 (0.014)	30.29/+5.36% (0.001)	28.77 (0.003)	30.30/ \pm 5.32% (0.001)

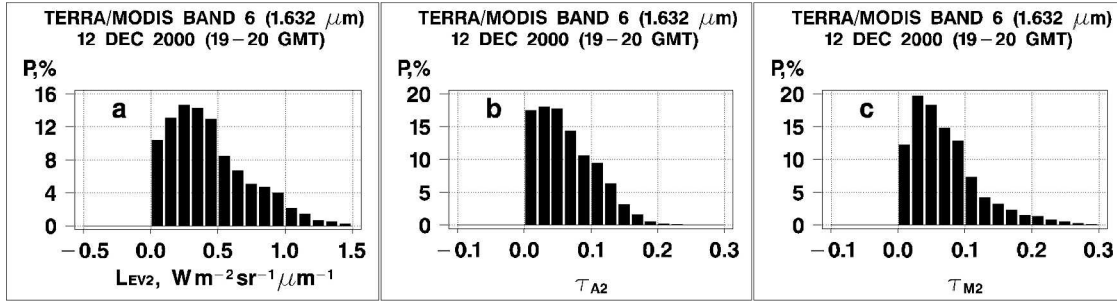


FIG. A2. Histogram of (a) aerosol radiance binned at $\Delta(L_{EV2}) = 0.1 \text{ W m}^{-2} \text{ sr}^{-1} \mu\text{m}^{-1}$ in *Terra*/MODIS band 6 at $1.632 \mu\text{m}$ as derived from one granule of CERES SSF data (1900–2000 UTC 12 Dec 2000). Truncation of negative radiances is done in the MODIS L1B processing; (b) A and (c) M τ retrievals (binned at $\Delta\tau = 0.02$). Note that the τ_A 's are *not* truncated in the A processing but appear truncated as a result of the L_{EV2} truncation, whereas the τ_M 's are truncated *in addition* to the L_{EV2} truncation.

nonlinearities. Additionally, the MODIS shortwave infrared bands 5–7 suffer from electronic cross-talk, out-of-band response (thermal leak; Ignatov 2003), and truncation of negative radiances as illustrated in Fig. A2. In addition to truncating radiances, the M-aerosol processing further truncates negative τ retrievals in contrast to the A-aerosol processing that allows negative τ retrievals to avoid data biases (Ignatov et al. 2004). The two former effects are substantially reduced in bands 5 and 7 on *Aqua*. It has been preliminarily observed that all MODIS bands on *Terra* have also been affected by electronics and power supply switches (section 3f). These effects are especially important for the aerosol size parameter, which is known to be extremely sensitive to even small calibration uncertainties (Ignatov et al. 1998; Ignatov 2002). Detailed information on the performance of MODIS instrument is found online at <http://www.mcst.ssai.biz/mcstweb/performance/>.

APPENDIX B

Mapping Specifics of the M- and A-Aerosol Products on CERES SSF Datasets

In the SSF processor, larger-resolution CERES FOVs ($\sim 20 \text{ km}$ at nadir) are used as “cookie cutters” for finer-resolution MODIS pixels ($\sim 1 \text{ km}$ at nadir; Geier et al. 2003). The respective CERES point spread-averaged statistics of MODIS radiances and geometries are then saved on the SSF, along with CERES radiances. Only CERES footprints with at least one MODIS pixel (as identified by the A processor, $N_{T,\min} = 1$) are retained on the SSF dataset, whereas footprints with no MODIS pixel are discarded. Likewise, if a MODIS pixel falls outside all CERES FOVs, it is excluded from calculation of the MODIS statistics and therefore not represented on the SSF. Finally, some CERES FOVs overlap so that some MODIS pixels may be counted more than once.

MODIS pixel count statistics in a CERES footprint, N_T , are defined by a *relative* footprint size of the two instruments. When both sensors point at nadir, the ratio

is $\sim (20 \text{ km} / 1 \text{ km})^2$ or ~ 400 , and it changes with the CERES and MODIS view zenith angles, θ_C and θ_M . Whether θ_C and θ_M are close or not depends on the mode in which the CERES instrument operates. MODIS always scans in a fixed azimuth plane (FAP) cross track (CT: scan plane is normal to the orbit plane) within $\sim \pm 55^\circ$ off-nadir, providing a 2330-km swath from an altitude of 705 km. CERES scans up to $\sim \pm 89^\circ$ and can operate in two basic modes: 1) FAP, two particular cases of which are CT and along track (AT: scan plane is coincident with orbit plane); and 2) rotated azimuth plane (RAP). When in a FAP/CT mode, CERES views the underlying surface almost simultaneously with MODIS at a very close view zenith angle: $\theta_C \approx \theta_M$. As a result, views from both instruments are constrained within $\theta \sim \pm 55^\circ$, and the size of a CERES footprint does not exceed $\sim 50 \text{ km}$. When in a FAP/AT mode, only near-nadir MODIS pixels are retained (i.e., $\theta_M \sim 0^\circ$), whereas the θ_C varies in a full range from 0° to 89° . At grazing angles (far backward/forward CERES views, which MODIS looks up a few minutes earlier/later than CERES), the size of a CERES footprint becomes quite large. The RAP mode is intermediate between the FAP/CT and FAP/AT modes.

A pair of CERES instruments onboard each platform is set to work in complementary modes. For instance, the *Terra* FM1 was in a FAP/CT mode during both weeks of December 2000 and June 2001, whereas the FM2 was in either RAP or FAP/AT mode. (A complete log of CERES operations is available from http://asd-www.larc.nasa.gov/dsnyder/Terra/terra_ops.html for *Terra* and from http://asd-www.larc.nasa.gov/dsnyder/Aqua/aqua_ops.html for *Aqua*.) The average footprint size for FM1 is thus expected to be smaller than for FM2. Figure B1 (top) shows histograms of total count, N_T , for December 2000 *Terra* MODIS pixels within those CERES FOVs with at least one valid aerosol observation. The N_T histogram for FM1 is highly asymmetric yet well constrained within $N_T \sim 300\text{--}550$. The FM2 histogram shows much similarity with FM1, except it includes footprints with much larger N_T . Su-

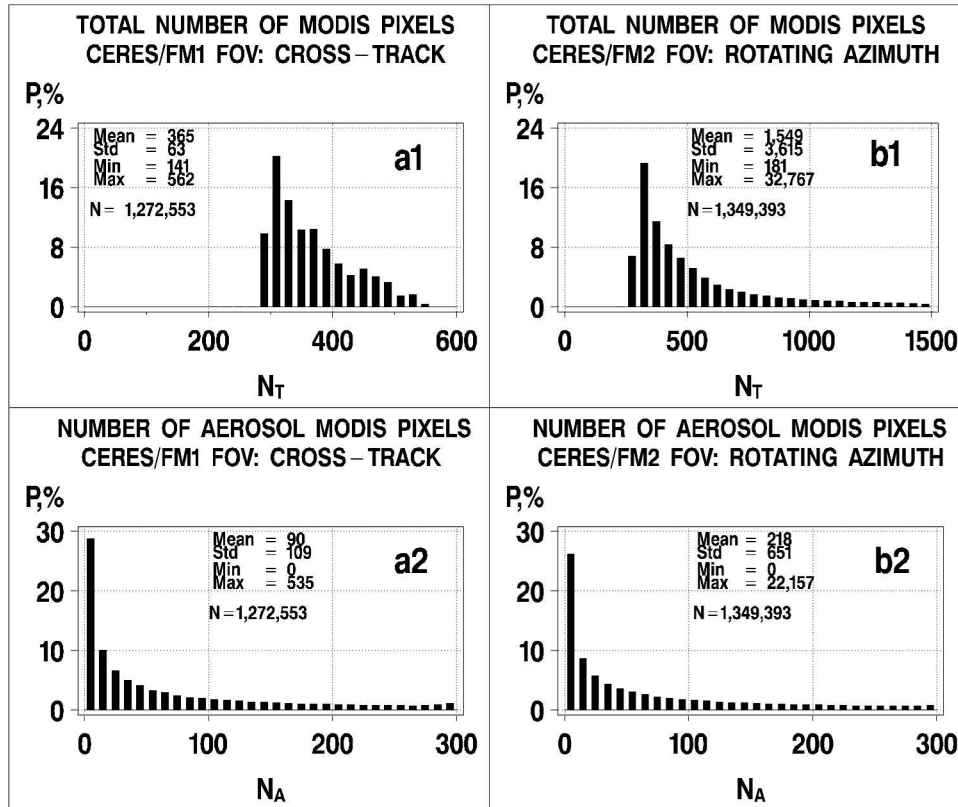


FIG. B1. Histograms of MODIS pixel count in a CERES footprint in Dec 2000: (a1), (b1) total, N_T ; (a2), (b2) aerosol, N_A ; (left) FM1; (right) FM2.

perimposed N_T statistics show that on average, $N_T = 365$ for FM1 and $N_T = 1549$ for FM2. These counts come from the A-product 1-km pixels, which are sampled in every other row and column, so that the actual number of 1-km MODIS pixels in a CERES

footprint is a factor of 4 larger. Minimum/maximum size of a CERES footprint can be evaluated as $a \sim 1 \text{ km} \times (4N_T)^{1/2}$. Substituting the respective $N_{T,\min}/N_{T,\max}$ from Fig. B1 for FM1, one obtains $a_{\min} \sim (4 \times 141)^{1/2} \sim 24 \text{ km}$ and $a_{\max} \sim (4 \times 562)^{1/2} \sim 47 \text{ km}$. For FM2,

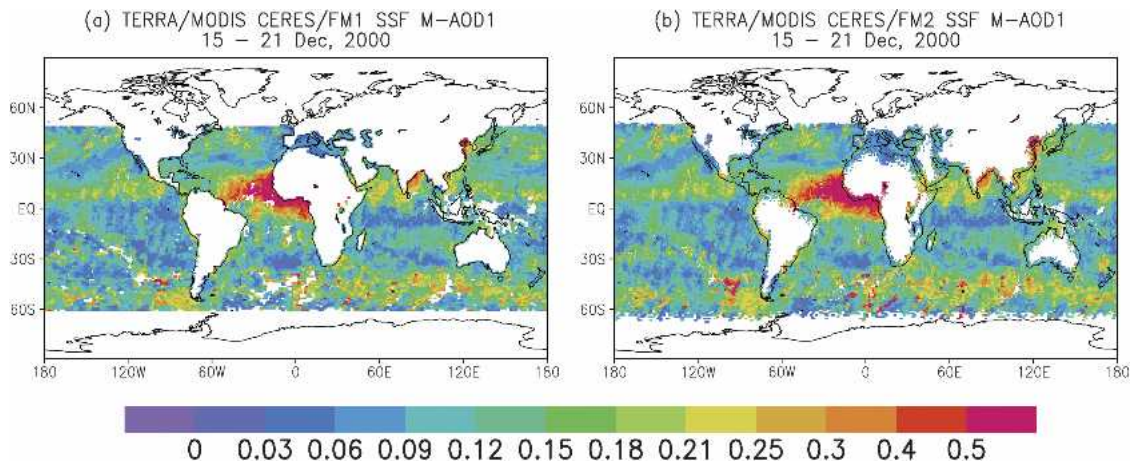


FIG. B2. Distribution of τ_{M1} (M product) over global ocean derived from *Terra* CERES SSF in Dec 2000: (a) FM1 (FAP/CT mode) and (b) FM2 (RAP mode). The increased blurriness in FM2 (b) is due to presence of large CERES footprints in the RAP data. (See discussion in section 3).

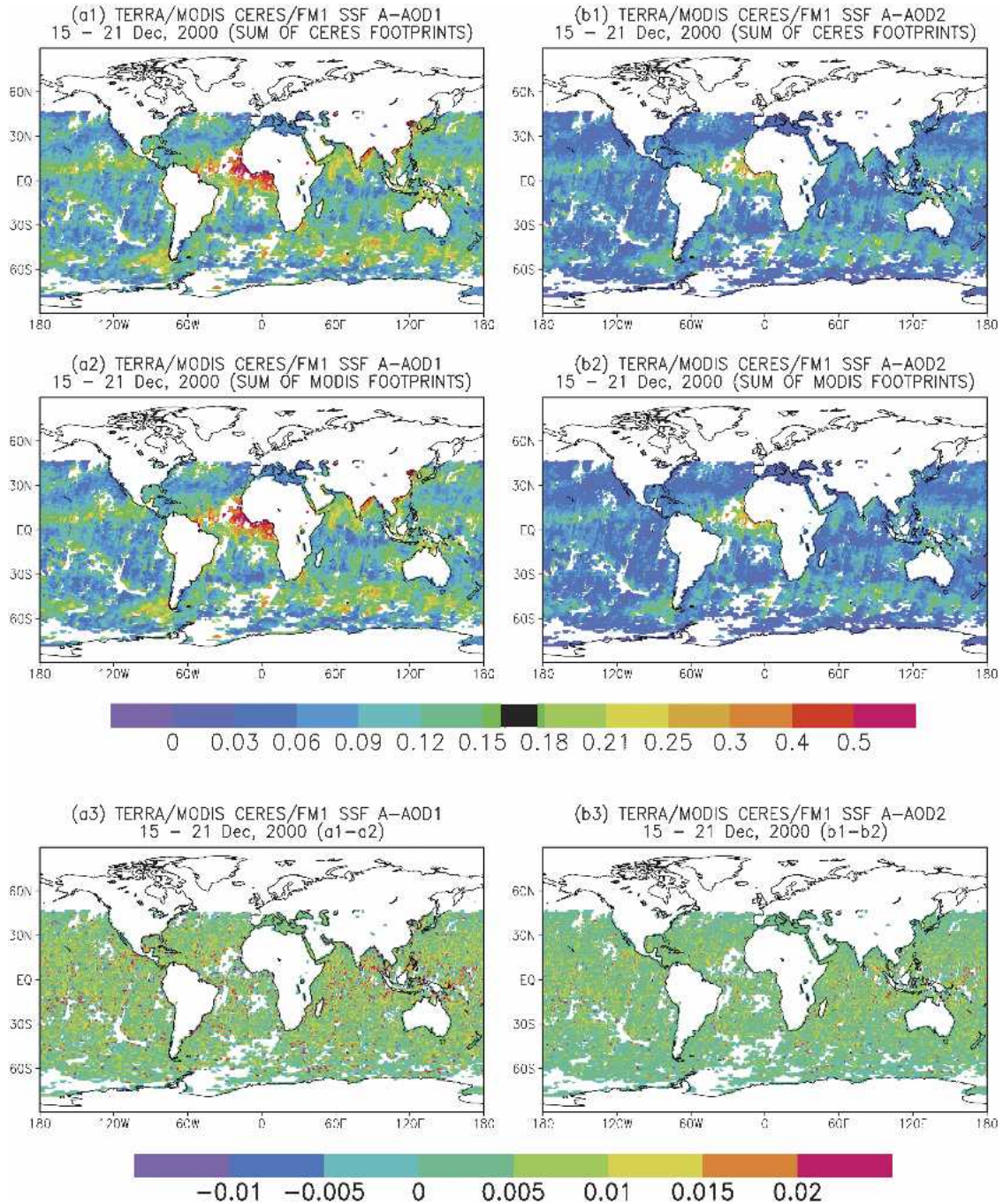


FIG. B3. Effect of different weighting on average (a) τ_{A1} and (b) τ_{A2} over $[7 \text{ day} \times (1^\circ)^2]$ boxes. 1) Each CERES footprint is given an equal weight; 2) each MODIS pixel is given an equal weight; 3) difference 2) minus 1). (Data of *Terra* CERES SSF FM1, Dec 2000.)

$a_{\min} \sim (4 \times 181)^{1/2} \sim 27 \text{ km}$ and $a_{\max} \sim (4 \times 32\,767)^{1/2} \sim 360 \text{ km}$.

In plotting Fig. B1, only those CERES footprints were considered with at least one valid aerosol observation (i.e., $N_A \geq 1$) from either the M or the A product. Shown in the second row of Fig. B1 are respective N_A histograms with superimposed statistics. [Note that

it is feasible that a CERES FOV may have $N_{A,\min}=0$. This occurs when a footprint contains M retrieval(s) but no A retrieval(s), or vice versa.] Again, there is much similarity between the FM1 and FM2 N_A histograms at the low-end N_A , but large differences at the high-end N_A . The CERES aerosol products are thus highly non-uniform in both spatial resolution and MODIS pixel

count within a footprint. The nonuniformities are especially noticeable when the CERES instrument is in a non-FAP/CT mode.

For large footprints, accurate geographical referencing of aerosol product may be problematic. (Recall that latitude and longitude are reported on the SSF at the center of a CERES FOV, which may be not representative of the location of aerosol cluster in it.) Figure B2 shows the global distribution of τ_{M1} (M product) for one week in December 2000 as derived from Terra CERES SSF FM1 (left) and FM2 (right). For mapping purposes, the aerosol retrievals reported on the SSF were first aggregated into $(1^\circ)^2$ grids and then averaged over the 7-day period, forming $N = 28\,578/28\,676$ [$7\text{ day} \times (1^\circ)^2$] boxes for the FM1/FM2, respectively. Close proximity of the two fields is expected as they represent but two different intermediate ways to map the original 10-km MOD04/MYD04 granules into [$7\text{ day} \times (1^\circ)^2$] boxes (via either FM1 or FM2 cookie cutters). Of interest is the increased “blurriness” in the FM2 map that is particularly evident in the vicinity of coastlines, around inland water bodies, and at the north/south boundaries at high latitudes. These “misplaced” $(1^\circ)^2$ boxes all come from the CERES/FM2 RAP footprints with large θ_c angles. The non-FAP/CT data should thus be used with caution.

The $7\text{ day} \times (1^\circ)^2$ boxes for Fig. B2 were obtained by triple averaging in the A product [FM1/FM2 cookie cutting, space averaging within $(1^\circ)^2$, and time averaging within 7 days] and quadruple averaging in the M product (MOD04/MY04 10-km processing, followed by the three steps listed above). In averaging CERES data within $(1^\circ)^2$, each CERES footprint was given an equal weight. Alternative to this approach is weighting each CERES FOV with number of MODIS aerosol pixels in it. (Note that this option is available for the A product only, as no N_T counterpart for the M product is saved on the SSF.) Figures B3a(1),a(2) and B3b(1), b(2) show τ_{A1} and τ_{A2} averaged two different ways, and Figs. B3a(3) and B3b(3) map their differences. The equal-weight (“CERES”) averaging tends to provide a slight positive bias that is typically a few thousandths of τ but may reach a few hundredths of τ in some areas. Different ways to average aerosol retrievals have been also used in some previous studies, for example, weighing each τ/α within a $(1^\circ)^2$ box in inverse proportion to its cloud amount (e.g., Mishchenko et al. 1999; Remer et al. 2002; REM). The effect is generally small in well-populated cloud-free areas but may be significant in poorly sampled cloudy areas. More analyses are needed to optimize the mapping procedure.

REFERENCES

- Ackerman, S., K. Strabala, P. Menzel, R. Frey, C. Moeller, and L. Gumley, 1998: Discriminating clear sky from clouds with MODIS. *J. Geophys. Res.*, **103**, 32 139–32 140.
- Ahmad, Z., and R. Fraser, 1982: An iterative radiative transfer code for ocean–atmosphere system. *J. Atmos. Sci.*, **39**, 656–665.
- Charlock, T., F. Rose, D. Rutan, D. Kratz, Z. Jin, L. Coleman, and Q. Fu, 2002: Relationship of tropical circulation and energetics using retrieved surface and atmospheric radiation budget (SARB) for January–August 1998. Preprints, *11th Conf. on Atmospheric Radiation*, Ogden, UT, Amer. Meteor. Soc., CD-ROM, 2.10.
- Cox, C., and W. Munk, 1954a: Measurement of the roughness of the sea surface from photographs of the sun’s glitter. *J. Opt. Sci. Amer.*, **44**, 838–850.
- , and —, 1954b: Statistics of the sea surface derived from sun glitter. *J. Mar. Res.*, **13**, 198–277.
- Geier, E., R. Green, D. Kratz, P. Minnis, W. Miller, S. Nolan, and C. Franklin, 2003: Clouds and the Earth’s Radiant Energy System (CERES) data management system: Single satellite footprint TOA/surface fluxes and clouds (SSF) collection document. Release 2, version 1, NASA Langley Research Center, 212 pp. and appendixes. [Available online at http://asd-www.larc.nasa.gov/ceres/collect_guide/SSF_CG.pdf.]
- Guzzi, R., J. Burrows, T. Kurosu, E. Cattani, M. Cervino, C. Levoni, and F. Torricella, 1998: GOME cloud and aerosol data products algorithm development. Final Report, ESA Contract 11572/95/NL/CN, 132 pp.
- Ignatov, A., 2002: Sensitivity and information content of aerosol retrievals from AVHRR: Radiometric factors. *Appl. Opt.*, **41**, 991–1011.
- , 2003: Spurious signals in the TRMM/VIRS reflectance channels and their effect on aerosol retrievals. *J. Atmos. Oceanic Technol.*, **20**, 1120–1137.
- , and N. Nalli, 2002: Aerosol retrievals from multiyear multisatellite AVHRR Pathfinder Atmosphere (PATMOS) dataset for correcting remotely sensed sea surface temperatures. *J. Atmos. Oceanic Technol.*, **19**, 2259–2277.
- , and L. Stowe, 2002a: Aerosol retrievals from individual AVHRR channels. Part I: Retrieval algorithm and transition from Dave to 6S radiative transfer model. *J. Atmos. Sci.*, **59**, 313–334.
- , and —, 2002b: Aerosol retrievals from individual AVHRR channels. Part II: Quality control, probability distribution functions, and consistency checks of retrievals. *J. Atmos. Sci.*, **59**, 335–362.
- , —, and R. Singh, 1998: Sensitivity study of the Ångström exponent derived from AVHRR over oceans. *Adv. Space Res.*, **21**, 439–442.
- , J. Sapper, I. Laszlo, N. Nalli, and K. Kidwell, 2004: Operational aerosol observations (AEROBS) from AVHRR/3 on board NOAA-KLM satellites. *J. Atmos. Oceanic Technol.*, **21**, 3–26.
- Kato, S., N. Loeb, and K. Rutledge, 2002: Estimate of top-of-atmosphere albedo for a molecular atmosphere over oceans using Clouds and the Earth’s Radiant Energy System (CERES) measurements. *J. Geophys. Res.*, **107**, 4396, doi:10.1029/2001JD001309.
- Kaufman, Y., D. Tanré, L. Remer, E. Vermote, A. Chu, and B. Holben, 1997: Operational remote sensing of tropospheric aerosol over land from EOS/MODIS. *J. Geophys. Res.*, **102**, 17 051–17 068.
- Levy, R., and Coauthors, 2003: Evaluation of the MODIS retrievals of dust aerosol over the ocean during PRIDE. *J. Geophys. Res.*, **108**, 8954, doi:10.1029/2002JD002460.
- Li, R.-R., Y. Kaufman, B.-C. Gao, and C. Davis, 2003: Remote sensing of suspended sediments and shallow coastal waters. *IEEE Trans. Geosci. Remote Sens.*, **41**, 559–566.
- Loeb, N., and S. Kato, 2002: Top-of-atmosphere direct radiative effect of aerosols over the tropical oceans from the Clouds and the Earth’s Radiant Energy System (CERES) satellite instrument. *J. Climate*, **15**, 1474–1484.
- Martins, J., D. Tanré, L. Remer, Y. Kaufman, S. Mattoo, and R. Levy, 2002: MODIS cloud screening for remote sensing of

- aerosols over oceans using spatial variability. *Geophys. Res. Lett.*, **29**, 8009, doi:10.1029/2001GL013252.
- MCST, 2000: MODIS level 1B product user's guide, for level 1B version 2.3.x, release 2. MCST Doc. PUG-01-U-DNCN, 57 pp. [Available online at <http://www.mcst.ssai.biz/mcstweb/L1B/product.html>.]
- , 2002a: MODIS level 1B product data dictionary. MCST Doc. MCM-02-2.3.1-PROC_L1BPDD-U-01-0107-REV B, MCST Internal Memo. M1039, 109 pp. [Available online at <http://www.mcst.ssai.biz/mcstweb/L1B/product.html>.]
- , 2002b: MODIS level 1B product user's guide, for level 1B version 4.0.9 (*Terra*) and version 4.1.1 (*Aqua*). MCST Doc. PUB-01-U-0202-REV B, MCST Internal Memo. M1038, 52 pp. [Available online at <http://www.mcst.ssai.biz/mcstweb/L1B/product.html>.]
- Minnis, P., D. Young, B. Wielicki, P. Heck, X. Dong, L. Stowe, and R. Welch, 1999: CERES cloud properties derived From multispectral VIRS data. *Proc. SPIE*, **3867**, 91–102.
- Mishchenko, M., I. Geogdzhayev, B. Cairns, W. Rossow, and A. Lacis, 1999: Aerosol retrievals over the oceans by use of channels 1 and 2 AVHRR data: Sensitivity analysis and preliminary results. *Appl. Opt.*, **38**, 7325–7341.
- Myhre, G., and Coauthors, 2004: Intercomparison of satellite retrieved aerosol optical depth over the ocean. *J. Atmos. Sci.*, **61**, 499–513.
- Remer, L., and Coauthors, 2002: Validation of MODIS aerosol retrievals over ocean. *Geophys. Res. Lett.*, **29**, 8008, doi:10.1029/2001GL013204.
- , and Coauthors, 2005: The MODIS aerosol algorithm, products, and validation. *J. Atmos. Sci.*, **62**, 947–973.
- Tanré, D., Y. Kaufman, M. Herman, and S. Matoo, 1997: Remote sensing of aerosol properties over oceans using the MODIS/EOS spectral radiances. *J. Geophys. Res.*, **102**, 16 971–16 988.
- Trepte, Q., Y. Chen, S. Sun-Mack, P. Minnis, D. F. Young, B. A. Baum, and P. W. Heck, 1999: Scene identification for the CERES cloud analysis subsystem. Preprints, *10th Conf. on Atmospheric Radiation*, Madison, WI, Amer. Meteor. Soc., 169–172.
- Vermote, E., D. Tanré, J. L. Deuze, M. Herman, and J. J. Morcrette, 1997: Second simulation of the satellite signal in the solar spectrum, '6S': An overview. *IEEE Trans. Geosci. Remote Sens.*, **35**, 675–686.
- Wielicki, B., B. Barkstrom, E. Harrison, R. Lee III, L. Smith, and J. Cooper, 1996: Clouds and the Earth's Radiant Energy System (CERES): An Earth Observing System experiment. *Bull. Amer. Meteor. Soc.*, **77**, 853–868.
- Xiong, J., J. Sun, J. Esposito, B. Guenther, and B. Barnes, 2002: MODIS solar reflectance bands calibration algorithm and on-orbit performance. *Proc. SPIE*, **4891**, 392–401.